

The Pennsylvania State University
The Graduate School

WIND ESTIMATION AND CLOSED-LOOP CONTROL OF A SOARING
VEHICLE

A Thesis in
Aerospace Engineering
by
John Bird

© 2013 John Bird

Submitted in Partial Fulfillment
of the Requirements
for the Degree of

Master of Science

December 2013

The thesis of John Bird was reviewed and approved* by the following:

Jacob W. Langelaan
Associate Professor of Aerospace Engineering
Thesis Advisor

Mark D. Maughmer
Professor of Aerospace Engineering

George A. Lesieutre
Professor of Aerospace Engineering
Department Head, Aerospace Engineering

*Signatures are on file in the Graduate School.

Abstract

Birds have demonstrated a remarkable ability to harvest energy from the atmosphere, allowing them to traverse vast regions foraging for food. From the thermalling flights of raptors and vultures to the astonishing flights of the albatross in the maritime wind shear birds have shown that their soaring ability is diverse and adaptable, making such techniques of interest for improving performance of small uninhabited air vehicles. This thesis investigates techniques to map the wind field surrounding an aircraft and then to exploit that wind field for energy. The wind fields and control techniques required for thermal and dynamic soaring in particular are studied. A system is developed that allows an aircraft with no knowledge of the wind field gather information, plan energy harvesting paths, and follow the required trajectory, and update the trajectory as information is gathered. In this way a loop is closed around the energy harvesting problem. Batch and hardware in the loop simulation is used to establish the capability of the system.

Table of Contents

| | |
|--|------------|
| List of Figures | vii |
| List of Tables | ix |
| Acknowledgments | x |
| Chapter 1 | |
| Energy Harvesting for Small Uninhabited Aerial Systems | 1 |
| 1.1 Intelligent Systems in Resource-Constrained Applications | 1 |
| 1.2 Energy Harvesting | 2 |
| 1.2.1 Static Soaring | 2 |
| 1.2.1.1 Thermal | 3 |
| 1.2.1.2 Wave | 3 |
| 1.2.1.3 Ridge or Slope | 4 |
| 1.2.2 Dynamic Soaring | 4 |
| 1.2.3 Gust Soaring | 6 |
| 1.3 A Control Architecture for Soaring | 6 |
| 1.4 Wind Modeling | 6 |
| 1.5 Contributions | 7 |
| 1.6 Readers Guide | 7 |
| Chapter 2 | |
| Vehicle and Environment Models | 8 |
| 2.1 Mapping, Planning, and Control for Soaring | 8 |
| 2.2 Vehicle Model | 8 |
| 2.2.1 Kinematic Thermalling Model | 9 |
| 2.2.2 Dynamic Soaring Equations of Motion | 10 |
| 2.2.3 Six Degree of Freedom Model for HiL Simulation | 12 |
| 2.3 Environmental Models | 13 |
| 2.3.1 Thermal Models | 14 |
| 2.3.2 Ridge Shear Model | 14 |
| 2.3.3 Turbulence Model | 15 |
| 2.4 Vehicle-Environment Interactions: Energy Harvesting | 16 |

| | | |
|------------------|---|-----------|
| 2.4.1 | The DS Rule and Shear | 16 |
| 2.4.2 | Direct Computation of Wind Field | 18 |
| Chapter 3 | | |
| | Wind Mapping | 21 |
| 3.1 | Kalman Filters, Estimation, and Wind Mapping | 21 |
| 3.2 | Mapping an <i>a priori</i> Determined Structure | 21 |
| 3.2.1 | Variability of the Mean Wind Field | 21 |
| 3.2.1.1 | Boundary Layer Shear | 22 |
| 3.2.1.2 | Ridge Shear | 22 |
| 3.2.2 | Modeling Wind Profiles With the Kalman Filter | 23 |
| 3.3 | Mapping Arbitrary Wind Structures | 24 |
| 3.3.1 | Spline Mathematics | 24 |
| 3.3.2 | Wind Mapping with Splines | 26 |
| 3.4 | Combined Model and Model-Free Wind Mapping | 27 |
| 3.5 | 1-D Mapping Results | 28 |
| 3.5.1 | Simulations | 28 |
| 3.5.2 | Fox Boundary-Layer Data | 28 |
| 3.5.3 | Ridge Shear Modeling Simulation | 29 |
| 3.6 | Mapping Multi-Dimensional Wind Structures | 30 |
| 3.6.1 | Thermal Simulation Results | 31 |
| Chapter 4 | | |
| | Optimizing Thermal Soaring | 33 |
| 4.1 | Thermal Contour Paths | 33 |
| 4.2 | Closed-loop Control | 34 |
| 4.3 | Simulation Results | 36 |
| 4.3.1 | Vehicle Model | 37 |
| 4.3.2 | Simulation Results | 37 |
| Chapter 5 | | |
| | Dynamic Soaring | 42 |
| 5.1 | Dynamic Soaring at Ridges | 42 |
| 5.2 | Control Architecture | 42 |
| 5.2.1 | Global Planner | 43 |
| 5.2.2 | Local Planner | 43 |
| 5.2.3 | Wind Mapper | 44 |
| 5.2.4 | Piccolo Communications | 44 |
| 5.3 | Global Planning | 44 |
| 5.4 | Closed-loop Control | 45 |
| 5.5 | DS Control with the Piccolo Autopilot | 47 |
| 5.6 | Hardware-in-the-Loop Simulations | 48 |
| 5.6.1 | Simulations in Smooth Air | 49 |
| 5.6.2 | Light Turbulence | 49 |
| 5.6.3 | Wind Mapper Performance | 52 |

| | |
|---|-----------|
| Chapter 6 | |
| Conclusions | 54 |
| 6.1 Use of Wind Maps in Energy Harvesting | 54 |
| 6.1.1 Static Soaring | 54 |
| 6.1.2 Dynamic Soaring | 54 |
| 6.2 Recommendations for Future Work | 55 |
| 6.2.1 Static Soaring and Wind Maps | 55 |
| 6.2.2 Closed-Loop Dynamic Soaring | 55 |
| Bibliography | 57 |

List of Figures

| | | |
|-----|--|----|
| 1.1 | Wandering albatross in flight. (JJ Harison 2012) | 2 |
| 1.2 | Lifecycle of thermals and cumulus clouds. Reproduced from the “Glider Flying Handbook” | 3 |
| 1.3 | Orographically induced lift sources. Ridge lift is mechanically generated while wave is a buoyant response to terrain forcing | 4 |
| 1.4 | Illustration of the principles of dynamic soaring energy harvesting as an aircraft crosses a zero order shear. In crossing the shear, inertial velocity remains the same while a step change occurs in airspeed, which the aircraft sees as an increase in kinetic energy. By reversing direction within a layer the aircraft can sustain flight indefinitely. | 5 |
| 2.1 | Autonomous dynamic soaring process. The aircraft starts by flying a mapping pattern (top), enters a dynamic soaring cycle (middle), and updates the trajectory as the wind map and aircraft speed evolves (bottom). | 9 |
| 2.2 | Coordinate frames used in modeling motion of DS aircraft. | 10 |
| 2.3 | Fox aircraft flying under power. From the Fox assembly manual. | 12 |
| 2.4 | Performance characteristics of the Escal Fox aircraft. | 13 |
| 2.5 | Gedeon thermal profiles. Type 1 has $C = 100\text{m}$, type 2 has $C = 40\text{m}$. In both cases strength is 1 m/s | 15 |
| 2.6 | Ridge Line Wind Profile with Spline Model, $w_{ref} = 8\text{ m/s}$, $\Delta h = 10\text{ m}$, and profile center at $h=5\text{ m}$ | 16 |
| 2.7 | Dryden turbulence model parameters for altitudes below 1000 ft AGL as specified by MIL-STD-1797A. | 17 |
| 2.8 | Dryden turbulence corrupted wind field with nominal velocity $u_{north} = 0\text{m/s}$, turbulence length $L_u = 43.8\text{m}$, variance $\sigma = 1.16\text{m/s}$. Reference wind $U_{20} = 6\text{m/s}$, reference altitude is 6m | 17 |
| 2.9 | Uncertainty in the wind measurements as a function of pitch angle for several angles of attack. | 20 |
| 3.1 | Power spectrum of horizontal winds, measured at Brookhaven National Laboratory. Reproduced from ”Power Spectrum of Horizontal Wind Speed in the Frequency Range from 0.0007 to 900 Cycles per Hour” [1] | 23 |
| 3.2 | Basis splines and one example spline with knots $[0, 0.25, 0.5, 0.75, 1]$, order 3 | 26 |
| 3.3 | Spline and parameter fit to boundary layer winds estimated from flight data during 18 Jan flight test. The aircraft was under manual control so the flight path was highly erratic, contributing to the noise seen in the wind measurements | 28 |

| | | |
|-----|---|----|
| 3.4 | Wind map estimates and $3 - \sigma$ confidence bounds for a 500 run Monte Carlo simulation series. Each run flies the same trajectory and is seeded with a random turbulence value of mean $\bar{U}_{20} = 9$ m/s and covariance of 3 m/s. All simulations are run with a shear of 6 m/s located between 100 m and 105 m, the true shear is indicated with thick lines. | 30 |
| 3.5 | Wind profile dependence on simulation time step size, the very sharp shear creates numeric difficulties as the aircraft crosses the shear layer. | 31 |
| 3.6 | Basis and a representative 2-dimensional tensor product spline. In this case knot distribution is uniform and identical in each direction, but this is not necessary. | 31 |
| 3.7 | Evolution of the thermal map for a type 2 thermal $w_0 = 4.4$ m/s, $C = 42.93$ m. Breaks in the outer ring are in regions not sampled by the sailplane. | 32 |
| 4.1 | Contours at several levels, illustrating the evolution of trajectory planning at several levels. The red trajectory is optimal at an airspeed of 14.8 m/s and achieves a mean climb rate of 0.86 m/s. | 35 |
| 4.2 | Illustration of Nonlinear guidance law from Park, et al | 35 |
| 4.3 | Park's Nonlinear Guidance Law Modified for Circular Trajectories | 36 |
| 4.4 | Flight paths for three thermalling techniques during a four minute simulation of an encounter with a type 1 thermal $C_0 = 3.2$ m/s, $R = 114.46$ m. | 38 |
| 4.5 | Climb rate during first and last 60 seconds of simulation in type 1 thermal. $C_0 = 3.2$ m/s, $R = 114.46$ m. The periodic notch in the planning method climb rate occurs on replanning as the aircraft maneuvers to intercept the new contour. | 39 |
| 4.6 | Flight paths for three thermalling techniques during a four minute simulation of an encounter with a type 2 thermal $C_0 = 4.4$ m/s, $R = 42.93$ m. | 40 |
| 4.7 | Climb rate during first and last 60 seconds of simulation in type 2 thermal. $C_0 = 4.4$ m/s, $R = 42.93$ m. | 41 |
| 5.1 | Closed loop dynamic soaring system components and communications pathways. | 43 |
| 5.2 | Feedforward-feedback control structure for dynamic soaring | 45 |
| 5.3 | Illustration of the Geometry of the Nonlinear Guidance Law | 46 |
| 5.4 | Dynamic soaring environment illustrating nominal flight path and acceleration, aircraft pose, and commands (exaggerated for clarity). Flight path is 55 seconds of simulation with shear thickness of 5 m, magnitude of 6 m/s, and no turbulence. | 50 |
| 5.5 | Nominal and actual state history for one dynamic soaring cycle. Cycle is planned to start at 24.8m/s in shear with $\Delta h = 5$ m, $w = 6$ m/s and no turbulence.. . . . | 51 |
| 5.6 | Flight path consistency measures, RMS error and energy change between adjacent cycles. Error is computed as the minimum distance between the aircraft location and a point on the flight path, RMS values are computed with a 1000 point sliding window. Simulation is initialized with $\Delta_z = 10$ m, $w=9$ m/s with no turbulence. At approximately $t=600$ seconds, light turbulence is turned on. | 52 |
| 5.7 | Time histories of wind map parameters for $\Delta_z = 5$ m, $w=6$ m/s, shear center is at 102.5 m. Turbulence is turned on at approx 650 seconds. Occasional spikes can be seen that appear to originate in the inter-process communication. Data starts when the dynamic soaring initialization command is issued and does not show wind map convergence prior to start. | 53 |

List of Tables

| | | |
|-----|---|----|
| 2.1 | Fox geometric and mass parameters. | 14 |
| 2.2 | Contributions of Largest Unmodeled Terms in Linear C_L Model to Estimated Angle of Attack | 18 |
| 2.3 | Uncertainty in the contributors to angle of attack estimation error | 19 |
| 3.1 | 2-D spline modeling errors from Monte-Carlo simulations. Each thermal type was simulated in 160 trials, some runs were excluded because the thermal core was very weak (less than 1 m/s) or because the aircraft failed to intercept the thermal. | 32 |
| 4.1 | Seed values used in generating thermals. Type 2 thermal radii refer to the radius of a single core (out of four). | 37 |
| 4.2 | Parameters for a simplified performance model of the RnR products SBXC sailplane. | 37 |
| 4.3 | Results for thermal exploitation of a type 1 thermal. | 38 |
| 4.4 | Results for thermal exploitation of type 2 thermals, averaged over 160 simulations. | 39 |
| 5.1 | Wind and turbulence simulation conditions used to test the DS controller, the center fields indicate the 20 foot wind parameter used to seed the turbulence magnitude. To vary turbulence independently of the shear strength, the 20 foot wind is treated solely as a turbulence parameter, not as a wind speed. | 48 |
| 5.2 | Dynamic soaring system performance with no turbulence. The 12 m/s condition typically failed after the Piccolo attitude filter diverged. (*-the wind map did not reach the convergence criterion before starting DS) | 49 |
| 5.3 | Dryden parameters for light turbulence. | 50 |
| 5.4 | Dynamic soaring system performance in light turbulence. The 12 m/s condition typically failed after the Piccolo attitude filter diverged. | 52 |

Acknowledgments

Corey Montella at Lehigh University was instrumental to this work, generating the trajectories and writing the backbone software to allow communication between the wind mapper, controller, and the Piccolo itself.

The support of my advisor, Jack Langelaan, has be phenomenal. Throughout this work, his insights have helped me to move forward on problems and understand both the problems I faced and occasionally the solutions I'd developed but not fully understood. From his initial task to develop the wind mapper, I've discovered an interest in autonomous exploration of the atmosphere.

In its entirety, the staff of the AVIA lab has made the transition to graduate school and to Penn State a joy. In particular Nate Deppenbusch and Sean Quinn Marlow have made my tenure a success, their insights and periodic excitement about some piece of this work has kept fresh the excitement of studying soaring flight.

Dedication

for all the birds who have taught me to fly

Energy Harvesting for Small Uninhabited Aerial Systems

1.1 Intelligent Systems in Resource-Constrained Applications

Originally deployed by military organizations, uninhabited aerial systems (UAS) are now being employed in such diverse roles as wildlife monitoring[2] and, severe weather surveillance[3, 4]. While there remain a number of regulatory and infrastructure barriers to widespread adoption of UAS for civilian applications, balancing cost and capability is a significant obstacle. One of the primary draws of uninhabited systems is the long-endurance missions made possible when an operator change is as easy as switching desks. Unfortunately the range and endurance required for many of these missions exceeds the capabilities of many small UAS, and in any case a trade must be made between sensing systems and fuel or batteries. Energy harvesting as a means to extend capability solely through intelligent control and exploitation of natural atmospheric phenomena is an attractive means to improve UAS capability.

Applications such as tracking endangered animals, geophysical and environmental field studies, and agriculture could benefit greatly from UAS. Many of these applications are also very cost-sensitive, precluding procurement of traditional high-capability aircraft which often have unit costs in excess of \$100 000 [5]. In order to contain costs these applications require aircraft, typically battery powered, bearing a strong resemblance in size and construction to model aircraft. Indeed, initial demonstrations of UAS use in these applications have used modified RC aircraft[2]. Such aircraft typically are very limited in endurance, often to less than 15 minutes. Use of intelligent systems to improve the performance of these systems could potentially allow dramatic improvements in performance while keeping procurement costs attainable for a variety of innovative applications.



Figure 1.1. Wandering albatross in flight. (JJ Harison 2012)

1.2 Energy Harvesting

Use of an awareness of the atmosphere and intelligent flight paths has given birds the ability to fly for long periods without significant energy expenditure. From the lazy circles of vultures and raptors, to the sweeping flight of the albatross, birds demonstrate an ability to harvest energy from the atmosphere at a variety of scales. Indeed, the largest birds all seem to exploit some form of atmospheric energy, enabling long foraging trips or migrations[6, 7, 8, 9].

As demonstrated by several researchers[10, 11, 12], energy harvesting for small UAS holds potential for dramatic improvements in performance. Energy harvesting from atmospheric phenomena is typically termed “soaring” in a nod to the sport where it was first explored [13]. Whether for sport or to improve the capability of UAS, soaring involves exploiting wind currents and their shears, using the energy of the atmosphere to power an aircraft. For engineering purposes, soaring is typically divided by the nature and scale of the phenomena exploited into static, dynamic, and gust soaring.

1.2.1 Static Soaring

Static soaring refers to the use of atmospheric updrafts whose vertical velocity offsets the descent rate of a sailplane. Exploited by a large variety of bird and insect species[14, 15], this was the first type of soaring to be widely understood. The clear mechanism for extracting energy and means to build instruments that guide pilots to exploitation of vertical movement led to rapid adoption of static soaring techniques. Use by manned aircraft dates as early as Orville Wright’s

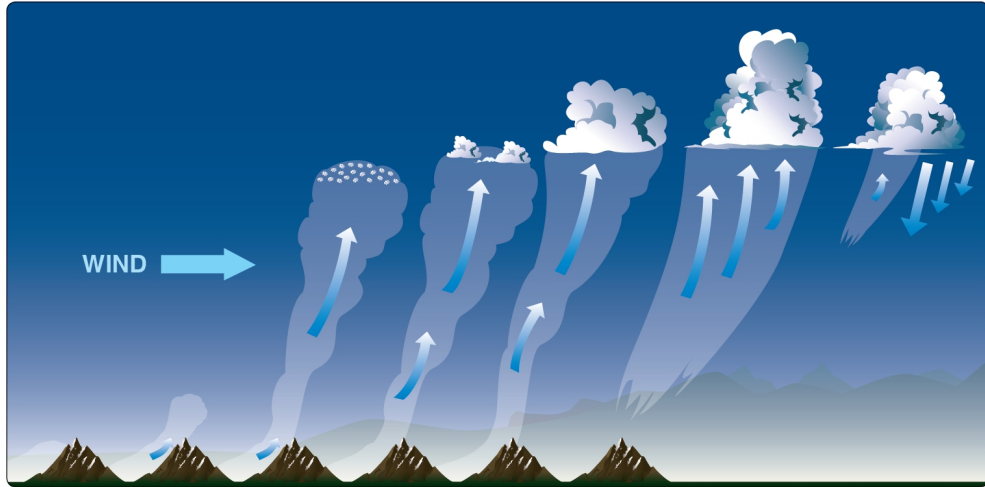


Figure 1.2. Lifecycle of thermals and cumulus clouds. Reproduced from the “Glider Flying Handbook”

flights in 1911, and static soaring continues to dominate modern sport soaring.

1.2.1.1 Thermal

The most widely used static soaring phenomena is thermals – rising columns of air made buoyant by solar heating of the surface (and thus the overlying air). Thermals are found throughout the world and a number of techniques for both manned and autonomous exploitation of thermals have been developed[11, 12, 16, 13], and autonomous systems have been demonstrated that exploit thermals to improve endurance[11] and cross-country range and speed[12]. Thermal soaring is however, limited to the boundary layer, typically within a few thousand meters of the surface and requires neutral stability in the lower troposphere to enable convection. Their roughly uniform distribution within regions of favorable conditions have made thermal exploitation computationally tractable, epitomized in MacCready’s speed to fly theory for optimal exploitation of thermal fields to maximize speed to a goal[17].

1.2.1.2 Wave

Wave phenomena form when a stably stratified layer of air is displaced vertically then oscillates under the influence of gravity about its level of neutral buoyancy. Typically found in the lee of mountain waves[18], wave can also be generated by wind shear though it is less predictable and infrequently used by human pilots[19]. Mountain lee waves can be powerful, long-lived, and exist over large geographic scales, so they are often employed in long-distance and record soaring by manned pilots. Vertically propagating waves can provide a sailplane access to the upper troposphere and lower stratosphere. While very powerful and long-lived, wave requires specific terrain features, a stable atmosphere, and significant winds and shear at the mountain top level[18]. This restricts usable wave to limited geographic regions and times of the year.

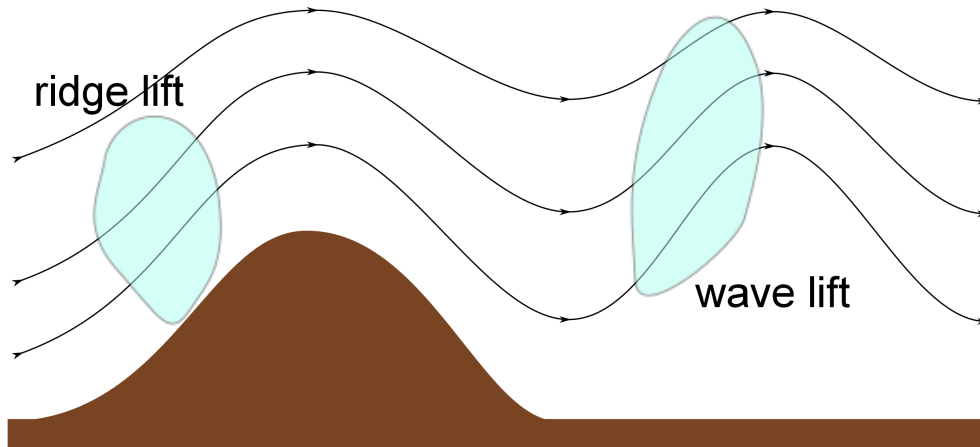


Figure 1.3. Orographically induced lift sources. Ridge lift is mechanically generated while wave is a buoyant response to terrain forcing

1.2.1.3 Ridge or Slope

Orographic lifting can provide updrafts along the face of steep terrain. Ridge lift will exist as long as wind strikes the terrain with sufficient speed and at an appropriate angle. As such, it can exist over very large areas, and is often used by birds and manned sailplanes. Routed planning for autonomous exploitation of ridge lift has been considered by Chakrabarty[20] in the ridge and valley terrain of central Pennsylvania. Similar to wave lift however, ridge is dependent upon the proper orography and winds.

1.2.2 Dynamic Soaring

Extraction of energy from spatial wind gradients has been termed dynamic soaring. Long observed in the behavior of albatrosses, Lord Rayleigh proposed the mechanism by which they sustain flight in 1898[15] seventy-five years later Klemperer provided a qualitative description of dynamic soaring trajectories[21]. Dynamic soaring remained unexplored from a mathematical perspective until Woods and Pennycuik revisited the dynamics of albatross flight, deriving the basic requirements of dynamic soaring behavior[22, 6]. In the 1980s pilots of radio-controlled sailplanes began exploiting wind gradients in the lee of ridges to achieve astonishing speeds, the record stands today at nearly 500 mph[23].

A reliable dynamic soaring system could dramatically improve the range and endurance of unmanned aircraft, the albatross can fly thousands of kilometers at a stretch by exploiting the shear over open ocean[7]. In a wildly different altitude range, shear surrounding the jet streams can reach values sufficient to sustain flight[24]. Dynamic soaring capability could thus open up both persistent, long range travel of the immediate surface region in maritime environments, and the upper troposphere.

Recent research in dynamic soaring has focused on planning energy exploiting trajectories for small UAS. In most cases path planning is cast as an optimization problem attempting to

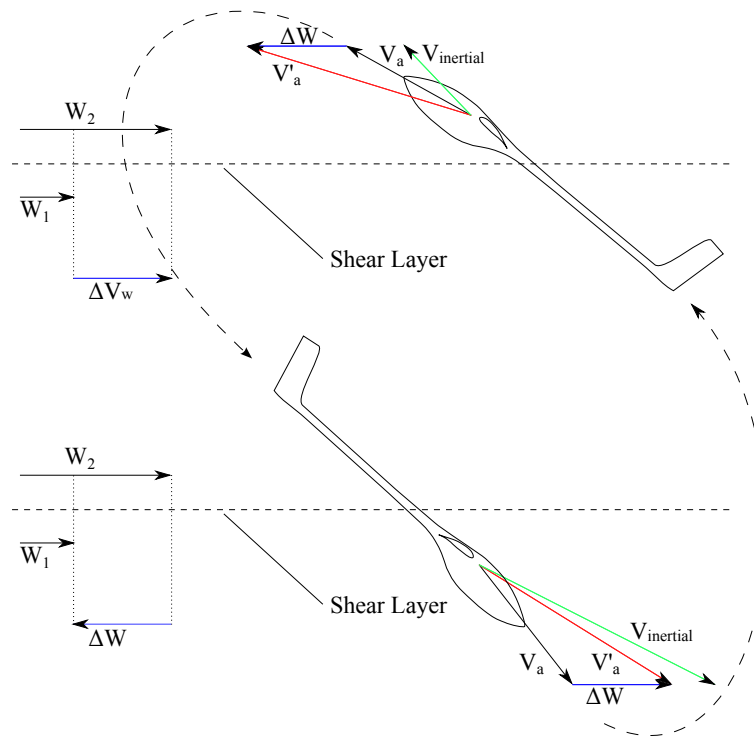


Figure 1.4. Illustration of the principles of dynamic soaring energy harvesting as an aircraft crosses a zero order shear. In crossing the shear, inertial velocity remains the same while a step change occurs in airspeed, which the aircraft sees as an increase in kinetic energy. By reversing direction within a layer the aircraft can sustain flight indefinitely.

minimize the wind speed or shear strength required to sustain flight, typically in the boundary layer or in linear shear layers[25, 24]. Sukumar[26] recasts the problem in an attempt to maximize the altitude of an aircraft flying in the boundary layer. Recognizing the need for adaptation to imperfectly flown trajectories, Flanzer[27] examines robust trajectory planning, minimizing the energy loss due to trajectory errors.

Computing the trajectories is typically accomplished using a collocation method where each optimization variable represents the aircraft state at a discrete point, and the equations of motion serve as nonlinear constraints between the two points[28, 29]. Differential flatness has also been explored to reduce computation time by Zhao[30], and later by Deittert[31] who obtains more reasonable results. Flanzer explores a direct computation method with a vortex lattice method, allowing surface deflections to be computed, he shows that the speed improvement over collocation and differential flatness planners is considerable[32].

Little work has been accomplished in system design or control of dynamic soaring aircraft. The “DS Rule,” [21, 22, 33] shows the basic requirements for a dynamic soaring controller, but little attention has been focused on the practical details of flying DS trajectories. Bowers identifies the components of a system needed for autonomous dynamic soaring, but does not build or test the system[34]. Demonstrations of autonomous aerobatic flight have been carried

out by Park[35], showing precise control when conducting accelerated maneuvers with extreme orientations. Gordon[36] developed a cueing system to assist human pilots in attempting to demonstrate dynamic soaring.

1.2.3 Gust Soaring

Similar to dynamic soaring, gust soaring exploits gradients in a wind field, temporal rather than shear. The idea of extracting energy from gusts originated with research into the effect of sinusoidal gusts on aircraft performance[37]. From this idea, a number of controllers have been developed to extract energy from gusts through longitudinal maneuvering in a random gust field[38, 39, 40]. Recently, Pennycuik has also been proposed that the albatross primarily uses gust rather than dynamic soaring, extracting energy from the separated regions behind ocean waves[41].

1.3 A Control Architecture for Soaring

To soar successfully, a controller is required that can take in information about the aircraft's environment and produce commands that will extract energy. For static soaring energy feedback laws[16] and circles centered on an estimate of the thermal position[11, 42] have been investigated. Each of these methods has been shown effective in extracting energy from thermals.

Soaring controls for dynamic and gust soaring have not been as rigorously explored. Receding horizon controllers have been investigated for gust soaring[40], but aside from the fuzzy rule based controller of Barate et al[43] no work has been accomplished in developing a system capable of dynamic soaring. While the fuzzy rule approach might allow dynamic soaring, integrating the ability to fly for a particular goal (such as station-keeping or travel) will require a more complex system. Such a system will need to unite an understanding of the local wind environment with a planner capable of generating trajectories to harvest energy from shear and a controller which can guide the aircraft on the appropriate path. Such a control architecture in principle has application to all modes of soaring, as each is concerned with the same three tasks.

1.4 Wind Modeling

In contrast to work on soaring techniques, relatively little effort has gone into enabling an aircraft to understand its local atmospheric environment. Gaussian or solenoidal circulation patterns have been used in simulation studies of soaring aircraft[44, 42], but these models have not been rigorously validated, and are chosen to represent features anecdotally observed by sailplane pilots. Konovalov[45, 46] develops two families of thermal models based on cross-sections flown through thermals, with Gedeon developing mathematical models that fit Konovalov's observations [47]. Modern sailplane instrumentation provides a rudimentary view of thermal structure to aid in maximizing climb rates[48], but functions primarily to identify the vague region of greatest lift.

The controller developed by Allen[11] and extended by Edwards[42] attempts to locate the center of a thermal by fitting a peak to a sliding window of climb rate measurements, but does not attempt to identify detailed structures of the windfield.

The literature is similarly sparse in modeling horizontal wind and shear fields. Langelaan[49] models the boundary layer environment using polynomial functions and a Kalman filter. This approach demonstrates a degree of modeling skill, but also finds that polynomials do not balance over fitting and description well, especially for large or complex domains. Several wind shear avoidance sensors also provide estimates of the wind shear environment, but this is limited to simply producing a “hazard index” to ward the pilot of a dangerous condition[50].

1.5 Contributions

This work presents a method to model atmospheric structures and controllers that can be used to exploit those structures for energy. Atmospheric modeling is presented in the context of mapping wind fields to support autonomous dynamic soaring and exploitation of thermals. Methods are presented to model fields with *a priori* determined structure, as well as arbitrary wind fields.

A candidate controller is presented for exploiting maps of convective updrafts. For dynamic soaring, a feedforward-feedback architecture is developed to linearize a dynamic soaring trajectory about a point and fly out path error with a feedback controller. Both applications make use of a non-linear feedback law for path following[35].

Energy harvesting for both static and dynamic soaring is evaluated in simulation. For dynamic soaring, a hardware in the loop simulation is used with a commercial, off the shelf autopilot system to establish the viability of dynamic soaring with currently available systems.

1.6 Readers Guide

- Chapter 2 describes the autonomous dynamic soaring problem and lays out foundational equations and models vehicles and then environment that are used throughout this work.
- Chapter 3 reviews the mathematics behind the wind models used and describes the wind modeling systems. Wind mapping results from simulation and flight experiments are presented, demonstrating the capability of the wind modeling system.
- Chapter 4 presents the use of wind maps for static soaring, and a planning method that exploits wind maps to maximize energy exploitation. Simulations comparing the mapping approach to traditional thermalling techniques is shown.
- Chapter 5 presents a dynamic soaring system incorporating wind maps, global planners, and local trajectory control that enables an autonomous aircraft extract energy from wind shear. Hardware in the loop simulation results demonstrate the capability to dynamic soar in selected environments.

Vehicle and Environment Models

2.1 Mapping, Planning, and Control for Soaring

The problem of primary interest in this work is the development of a system capable of autonomously dynamic soaring, specifically in the separated flow region behind ridges. The system should have a number of capabilities.

- Take off with no knowledge of the winds.
- Fly a pattern to gather information on the wind field structure, and identify when sufficient information has been gathered to begin dynamic soaring.
- Identify a suitable trajectory, enter, and sustain a dynamic soaring cycle in the mapped shear environment.
- Update the wind map and trajectory while dynamic soaring as more information is gathered and the wind field evolves.

An illustration of this process is shown in Figure 2.1. While this process is described here in the context of dynamic soaring, the mapping, exploitation, and replanning cycle is relevant to any form of atmospheric energy harvesting. Application of this process to static soaring is also developed and presented. First, the foundational vehicle and environmental models used throughout this work will be presented.

2.2 Vehicle Model

Several vehicle models were used in a number of simulations. Fidelity ranges from two dimensional kinematics to a six degree of freedom model using extensive lookup tables for aerodynamic forces and moments.

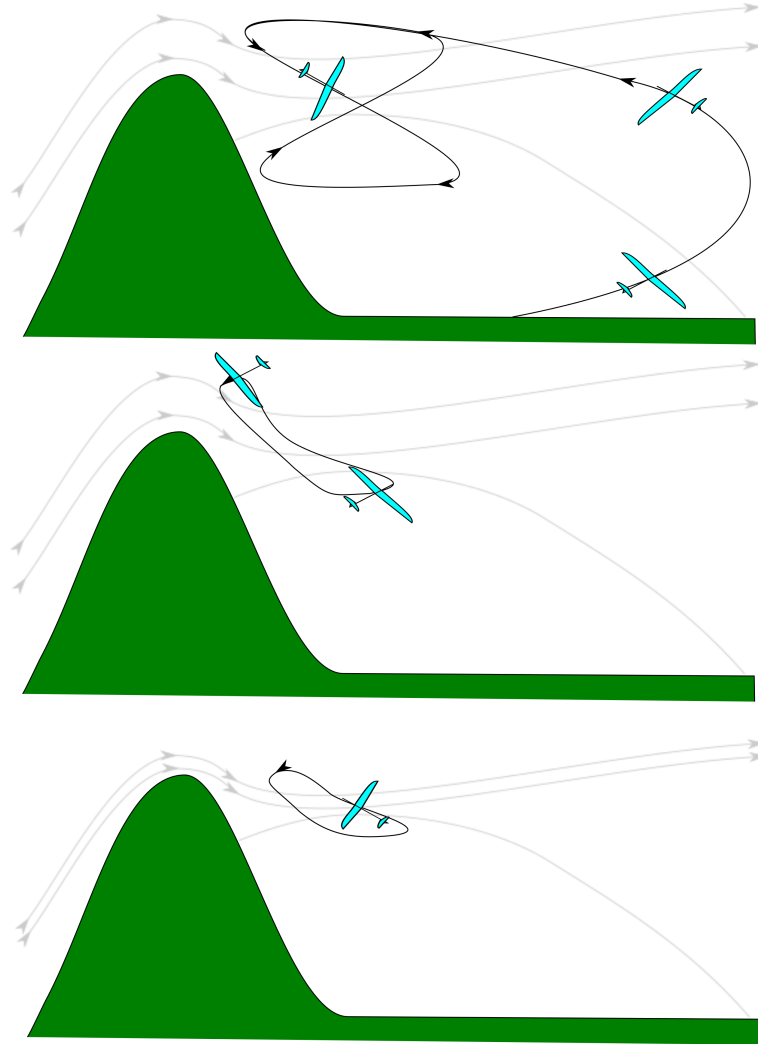


Figure 2.1. Autonomous dynamic soaring process. The aircraft starts by flying a mapping pattern (top), enters a dynamic soaring cycle (middle), and updates the trajectory as the wind map and aircraft speed evolves (bottom).

2.2.1 Kinematic Thermalling Model

For thermal modeling and exploitation, only the aircraft's location in a 2-d plane through the thermal is important as thermals are assumed not to vary with height. A simple kinematic model is then all that is required to assess thermalling performance and determine aircraft state. States for the model are $(x, y, \psi, \dot{\psi})$; position, heading, and heading rate. Speed is assumed to be constant and a single control variable is used – lateral acceleration. The equations of motion are expressed:

$$\dot{\mathbf{X}} = \begin{bmatrix} \dot{x} \\ \dot{y} \\ \dot{\psi} \\ \ddot{\psi} \end{bmatrix} = \begin{bmatrix} V \cos \psi \\ V \sin \psi \\ \dot{\psi} \\ 0 \end{bmatrix} + \begin{bmatrix} 0 \\ 0 \\ 0 \\ \frac{U}{V} \end{bmatrix} \quad (2.1)$$

Where U is the lateral acceleration command.

To evaluate the climb performance of thermalling gliders it is important to account for the effect of load factor on sink rate, so a performance model augments the vehicle dynamic equations. This is accomplished by computing the load factor for a steady turn with the specified lateral acceleration:

$$n = \sqrt{U^2 + g^2} \quad (2.2)$$

Assuming that altitude varies little so that a fixed air density can be used, and with a few aircraft parameters specified the lift coefficient can be computed and a lookup table specifying the aircraft polar allows the sink rate to be determined. The simulation is implemented in MATLAB using a Runge-Kutta fourth order integration.

2.2.2 Dynamic Soaring Equations of Motion

In path planning for dynamic soaring, a three degree of freedom point mass model is typically employed[29]. Derivation of these equations begins with several coordinate frames: an inertial north-east-down frame fixed to the earth, a frame carried by the wind, and a vehicle fixed stability frame which has it's x-axis pointed in the direction of flight.

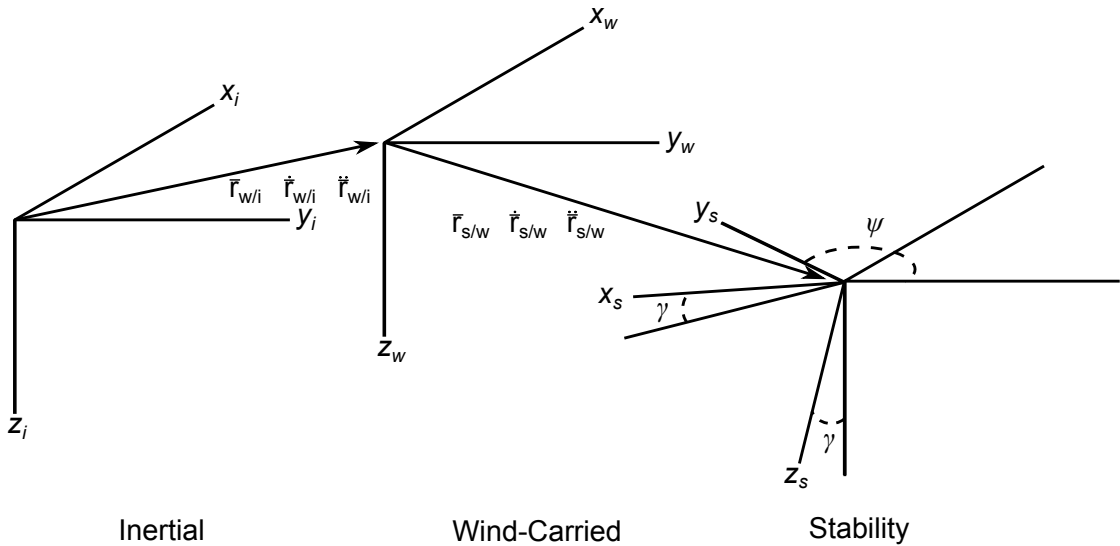


Figure 2.2. Coordinate frames used in modeling motion of DS aircraft.

The aircraft position can be expressed as the sum of position vectors:

$$\mathbf{r}_{s/i}^i = \mathbf{r}_{w/i}^i + \mathbf{r}_{s/w}^i \quad (2.3)$$

Adopting the notation of Stephens and Lewis[51], where $\frac{{}^s \partial x_{a/b}^t}{\partial t}$ indicates the partial derivative taken in the s fraome of the vector x , measured between a and b , whose components are expressed in the t frame. An inertial derivative with respect to time is taken of the position:

$$\frac{{}^i \partial \mathbf{r}_{s/i}^i}{\partial t} = \dot{\mathbf{r}}_{s/i}^i = \boldsymbol{\omega}_{w/i} \times \mathbf{r}_{w/i}^i + \dot{\mathbf{r}}_{w/i}^i + \boldsymbol{\omega}_{s/w} \times \mathbf{r}_{s/w}^i + \dot{\mathbf{r}}_{s/w}^i \quad (2.4)$$

Rewriting $\mathbf{r}_{w/i}^i$ as \mathbf{W} , noting that $\boldsymbol{\omega}_{w/i} = \mathbf{0}$ considering an instant where O_s and O_w are coincident so that $\mathbf{r}_{s/w}^i = \mathbf{0}$:

$$\dot{\mathbf{r}}_{s/i}^i = \mathbf{W} + \dot{\mathbf{r}}_{s/w}^i \quad (2.5)$$

Taking another derivative:

$$\frac{{}^i \partial \dot{\mathbf{r}}_{s/i}^i}{\partial t^2} = \ddot{\mathbf{r}}_{s/i}^i = \boldsymbol{\omega}_{w/i} \times \mathbf{W} + \dot{\mathbf{W}} + \boldsymbol{\omega}_{s/w} \times \dot{\mathbf{r}}_{s/w}^i + \ddot{\mathbf{r}}_{s/w}^i \quad (2.6)$$

Noting again, that $\boldsymbol{\omega}_{w/i} = \mathbf{0}$ and transforming to stability frame:

$$\mathbf{R}_{s/i} \ddot{\mathbf{r}}_{s/i}^i = \frac{\mathbf{R}_{s/i} \mathbf{F}}{m} = \mathbf{R}_{s/i} \dot{\mathbf{W}} + \boldsymbol{\omega}_{s/w} \times \dot{\mathbf{r}}_{s/w}^s + \ddot{\mathbf{r}}_{s/w}^s \quad (2.7)$$

Where $\dot{\mathbf{r}}_{s/w}^s = [V_a, 0, 0]^T$. Taking the bank angle, μ , to be an input so that it's dynamics need not be handled explicitly then $\mathbf{R}_{s/i}$ can be expanded:

$$\mathbf{R}_{s/i} = \begin{bmatrix} \cos \gamma \cos \psi & \cos \gamma \sin \psi & -\sin \gamma \\ -\sin \psi & \cos \psi & 0 \\ \sin \gamma \cos \psi & \sin \gamma \sin \psi & \cos \gamma \end{bmatrix} \quad (2.8)$$

Rotating the angular velocity $\boldsymbol{\omega}_{s/w}$ to stability frame:

$$\boldsymbol{\omega}_{s/w}^s = \begin{bmatrix} \cos \gamma & 0 & -\sin \gamma \\ 0 & 1 & 0 \\ \sin \gamma & 0 & \cos \gamma \end{bmatrix} \begin{bmatrix} 0 \\ \dot{\gamma} \\ \dot{\psi} \end{bmatrix} = \begin{bmatrix} -\sin \gamma \dot{\psi} \\ -\dot{\gamma} \\ \cos \gamma \dot{\psi} \end{bmatrix} \quad (2.9)$$

Substituting into Equation 2.7 and expanding the force and wind terms:

$$\begin{aligned} -\frac{D}{m} - g \sin \gamma &= \dot{V}_a + \dot{W}_x \cos \gamma \cos \psi + \dot{W}_y \cos \gamma \sin \psi - \dot{W}_z \sin \gamma \\ \frac{L}{m} \sin \mu &= V_a \dot{\psi} \cos \gamma - \dot{W}_x \sin \psi + \dot{W}_y \cos \psi \\ -\frac{L}{m} \cos \mu + g \cos \gamma &= -V_a \dot{\gamma} + \dot{W}_x \sin \gamma \cos \psi + \dot{W}_y \sin \gamma \sin \psi + \dot{W}_z \cos \gamma \end{aligned} \quad (2.10)$$

Assuming that the wind is in the horizontal plane only, and rearranging for the state derivatives:

$$\begin{aligned}
\dot{V}_a &= -d - g \sin \gamma - \dot{W}_x \cos \gamma \cos \psi - \dot{W}_y \cos \gamma \sin \psi \\
\dot{\psi} &= l \sin \mu + \dot{W}_x \sin \psi - \dot{W}_y \cos \psi \\
\dot{\gamma} &= l \cos \mu - g \cos \gamma + \dot{W}_x \sin \gamma \cos \psi + \dot{W}_y \sin \gamma \sin \psi
\end{aligned} \tag{2.11}$$

The navigation equations given in Equation 2.5 can be rewritten in terms of V_a , giving:

$$\dot{\mathbf{r}}_{s/i}^i = \begin{bmatrix} \dot{North} \\ \dot{East} \\ \dot{Down} \end{bmatrix} = \begin{bmatrix} W_n \\ W_e \\ W_d \end{bmatrix} + \begin{bmatrix} V_a \cos \gamma \cos \psi \\ V_a \cos \gamma \sin \psi \\ -V_a \sin \gamma \end{bmatrix} \tag{2.12}$$

Equations 2.11 and 2.12 then fully specify the motion of a dynamic soaring aircraft whose rotational dynamics are assumed to be slow enough to be neglected, and that flies with no sideslip angle. While restrictive, these assumptions are realistic for ideal DS paths – to maximize efficiency it is desirable to fly coordinated (i.e. without sideslip), and dynamic soaring paths tend to be smooth which reduces the effect of the rotational dynamics.

2.2.3 Six Degree of Freedom Model for HiL Simulation

For hardware in the loop simulation, the Piccolo HiL simulation is used. This implements a six degree of freedom aircraft simulation that runs in real time and allows specification of a wind profile and aircraft model. The aircraft model is specified using lookup tables for stability derivatives as a function of angle of attack. Stability axis force coefficients and body axis moment coefficients are constructed as a function of angle of attack, sideslip, non-dimensional body rates, and surface deflections. The aircraft dynamics are computed on a spherical Earth and states communicated to the Piccolo using CAN bus.



Figure 2.3. Fox aircraft flying under power. From the Fox assembly manual.

The aircraft platform for dynamic soaring experiments is the Escale Fox, a 2.8 m span scale model of the Fox aerobatic sailplane. The Fox is chosen as it offers large control surfaces for agility, a high aspect ratio wing, auxiliary propulsion system for launching, and has enough internal volume for the Piccolo and dynamic soaring system. It is of conventional configuration, with relatively high aspect ratio wings and a cruciform tail, pictured in Figure 2.3[52]. The aircraft geometry was measured and used to construct a model of the aircraft for the vortex lattice software AVL. A software tool was written to automatically run AVL at a series of angles

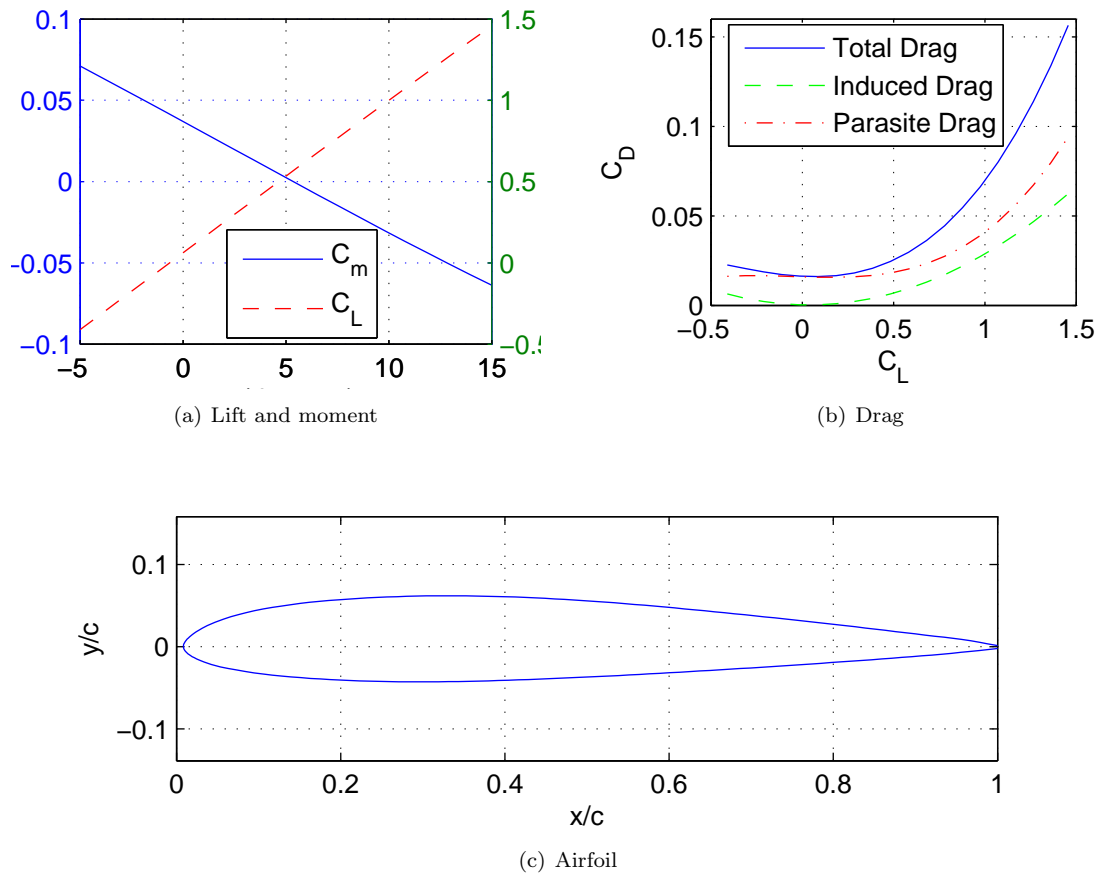


Figure 2.4. Performance characteristics of the Escala Fox aircraft.

of attack and parse the resulting stability derivatives.

As airfoil data is not available for the model, a trace of the wing root was taken and digitized (Figure 2.4(c)). The airfoil profile was then reconstructed and airfoil characteristics were computed using Xfoil at a chord Reynolds number of 400,000. Airfoil characteristics were combined with the AVL results, a wetted area drag buildup, and an estimate of the fuselage drag coefficient to generate the aircraft drag polar. The resulting aircraft performance characteristics are shown in Figure 2.4 while key aircraft parameters are in Table 2.1.

2.3 Environmental Models

For testing the models developed to characterize the atmospheric environment, models of the phenomena of interest are required. Of particular interest in this work are models of wind shear, convective updrafts, and turbulence.

| Parameter | Value |
|--------------------|-------------------------|
| S | 0.634 m ² |
| \bar{c} | 0.226 m |
| b | 2.8 m |
| m | 4 kg |
| J _x | 0.729 kg-m ² |
| J _y | 0.343 kg-m ² |
| J _z | 1.07 kg-m ² |
| J _{xz} | 0.0 kg-m ² |
| L/D _{max} | 19.7 |

Table 2.1. Fox geometric and mass parameters.

2.3.1 Thermal Models

A number of thermal models have been proposed based on limited measurements of thermals and heuristically based on the experience of glider pilots. In general they all share a central core region, surrounding the core an area where the updraft velocity drops rapidly, and an outer region with slight sink (downward moving air) surrounding the thermal. The strength of the central core, its width, and the shear strength between core and surrounding varies widely between models however.

Based on aircraft interceptions of a number of thermals, Konovalov provides two conceptual thermal models, one with a single peak and another with a wider “flat” top with sharply dropping lift surrounding[45, 46]. Gedeon formalizes these models with mathematical descriptions the type 1 thermal with a Gaussian shape and the type 2 “flat” topped thermal as a composition of several Gaussians[47]. The type 1 is described:

$$w = w_0 e^{-\left(\frac{c}{\bar{c}}\right)^2} \left[1 - \left(\frac{c}{C}\right)^2 \right] \quad (2.13)$$

While the type 2 is given:

$$w = w_{c0} \left\{ \frac{13}{11} e^{-\left(\frac{c+2C}{\bar{c}}\right)^2} \left[1 - \left(\frac{c+2C}{C}\right)^2 \right] + \frac{4}{3} e^{-\left(\frac{c+\frac{2}{3}C}{\bar{c}}\right)^2} \left[1 - \left(\frac{c+\frac{2}{3}C}{C}\right)^2 \right] + \dots \right. \\ \left. \frac{4}{3} e^{-\left(\frac{c-\frac{2}{3}C}{\bar{c}}\right)^2} \left[1 - \left(\frac{c-\frac{2}{3}C}{C}\right)^2 \right] + \frac{13}{11} e^{-\left(\frac{c-2C}{\bar{c}}\right)^2} \left[1 - \left(\frac{c-2C}{C}\right)^2 \right] \right\} \quad (2.14)$$

Where c is the radial position in the thermal and C is a radial size parameter. Figure 2.5 shows a cross-section of both thermal types.

2.3.2 Ridge Shear Model

While the separated flow region behind ridge lines is commonly used by RC dynamic soaring pilots, a comprehensive investigation of its structure has not been undertaken. In the absence

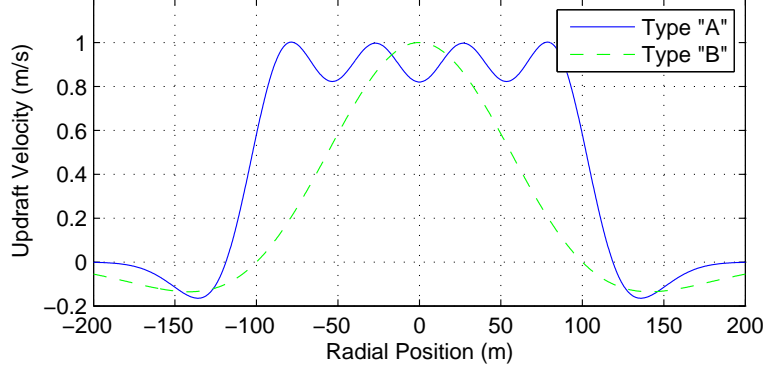


Figure 2.5. Gedeon thermal profiles. Type 1 has $C = 100\text{m}$, type 2 has $C = 40\text{m}$. In both cases strength is 1 m/s

of a rigorous characterization of the profile, some consideration of the origin and limiting characteristics of the shear can be used to develop a working model. After separation from the hill, the shear region will initially preserve the original boundary layer profile above the separation streamline. As the flow continues, shear below the separation streamline will mix the quiescent region into a boundary layer as well. Thus, the shear will qualitatively resemble a boundary layer reflected about a central streamline. Logistic functions describe this shape, and so were used in this investigation to represent the separated wind profile in the lee of a ridge. In particular:

$$w(z) = \frac{w_{ref}}{1 + e^{\frac{14}{\Delta h}(\frac{\Delta h}{2} - (z - h_0))}} \quad (2.15)$$

Where w_{ref} is the speed increment across the shear, Δh is the thickness of the shear layer, and h_0 is the bottom of the layer. The profile is depicted in Figure 2.6.

2.3.3 Turbulence Model

In order to assess the effect of atmospheric turbulence on dynamic soaring controllers, some form for the turbulence must be adopted. The Dryden turbulence model describes turbulence as a stationary Gaussian process[53]. It makes a “frozen wave” assumption – that is the wind field is assumed to be static and the aircraft flies through this field. The Dryden spectra is specified[54]:

$$\begin{aligned} \phi_u(\omega) &= \frac{2\sigma_u^2 L_u}{\pi \left((L_u \omega)^2 + 1 \right)} \\ \phi_v(\omega) &= \frac{\sigma_v^2 L_v \left(1 + 3(L_v \omega)^2 \right)}{\pi \left(1 + (L_v \omega)^2 \right)^2} \\ \phi_w(\omega) &= \frac{\sigma_w^2 L_w \left(1 + 3(L_w \omega)^2 \right)}{\pi \left(1 + (L_w \omega)^2 \right)^2} \end{aligned} \quad (2.16)$$

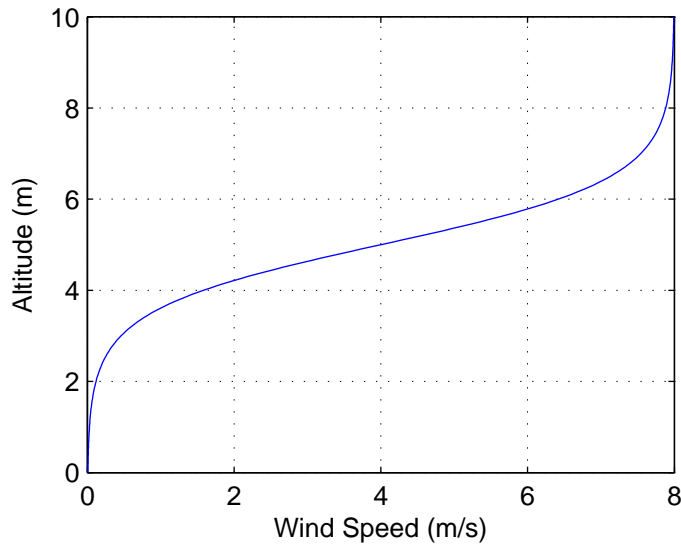


Figure 2.6. Ridge Line Wind Profile with Spline Model, $w_{ref} = 8$ m/s, $\Delta h = 10$ m, and profile center at $h=5$ m

MIL-STD-1797A provides definitions of the turbulence length and intensity for low-altitude regions (below 1000 ft)[54], giving vertical gust intensity (standard deviation) as 10% of the 20-foot wind magnitude. Horizontal intensity is defined as fractions of σ_w

$$\frac{\sigma_u}{\sigma_w} = \frac{\sigma_v}{\sigma_w} = \frac{1}{(0.177 + 0.000823z)^{0.4}} \quad (2.17)$$

Where z is specified in feet. Turbulence length scales are also defined – vertical length scale is equal to the aircraft altitude, and horizontal scales are again given as functions of height.

$$L_u = L_v = \frac{z}{(0.177 + 0.000823z)^{1.2}} \quad (2.18)$$

Again, z and L are given in feet. Figure 2.8 illustrates a sample of the resulting gust field for a dynamic soaring vehicle operating at low altitudes with a mean wind speed of 6 m/s. Turbulence intensity and length scales are shown graphically in Figure 2.7.

2.4 Vehicle-Environment Interactions: Energy Harvesting

2.4.1 The DS Rule and Shear

The basic requirements for closed dynamic soaring cycles were described by Klemperer[21], indicating that climbs against the wind and dives with it could be connected by turns to sustain flight. This was formalized by Wood who computed the energy gains for various climb angles[22] and Boslough who termed the relationship between climbs/dives and energy harvesting the “Dynamic Soaring Rule” [33]. For vertical shear of the horizontal wind the rule is that an aircraft

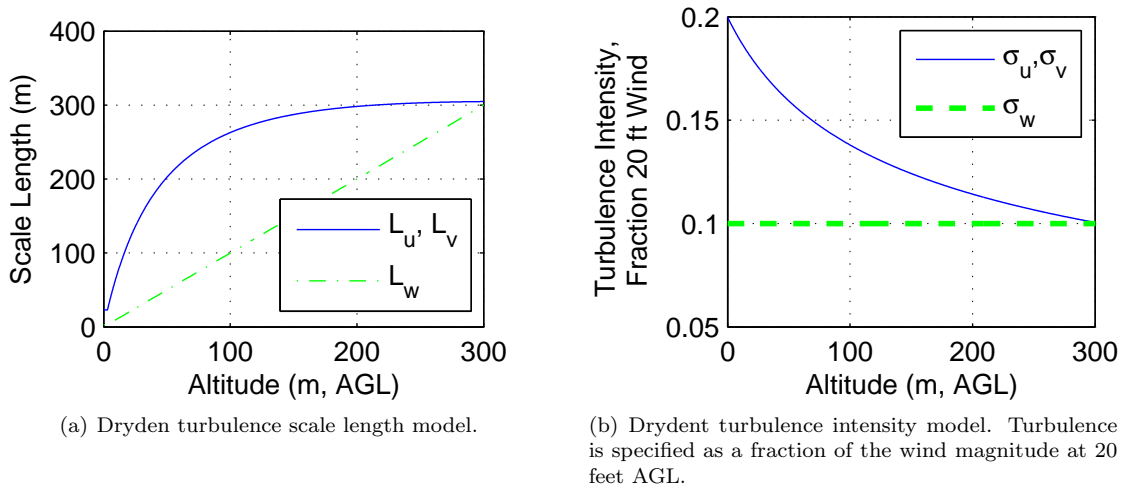


Figure 2.7. Dryden turbulence model parameters for altitudes below 1000 ft AGL as specified by MIL-STD-1797A.

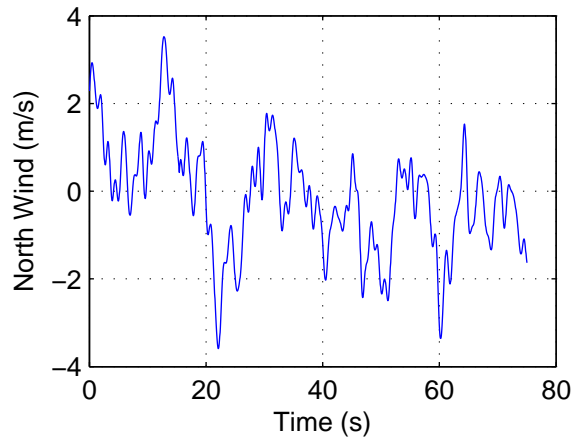


Figure 2.8. Dryden turbulence corrupted wind field with nominal velocity $u_{north} = 0\text{m/s}$, turbulence length $L_u = 43.8\text{m}$, variance $\sigma = 1.16\text{m/s}$. Reference wind $U_{20} = 6\text{m/s}$, reference altitude is 6m

must climb into the shear and dive out of it, energy extraction is maximized when the flight path is at a 45° angle to the horizontal.

A more general treatment of the effect of the shear can be obtained by considering the gradient as a time derivative of wind (indeed as it originally enters the aircraft equations of motion). Examining Equation 2.10, it can be seen that the airspeed is increased if the time derivative of the wind component in the direction of flight is positive, i.e. the dot product of the aircraft velocity and wind derivative is negative.

$$\dot{V}_a = -\dot{\mathbf{W}} \cdot \mathbf{V}_a \quad (2.19)$$

2.4.2 Direct Computation of Wind Field

The method of direct wind field computation described by Langelaan et al. is used in this paper to generate wind measurements for the modeling algorithms[55]. To generate a wind measurement, a vector difference is taken between the inertial velocity and air-relative velocity. Computing this difference requires that the aircraft wind-relative velocity be known in an inertial frame. Since the wind angles α and β are typically not measured on most aircraft, an acceptable means to approximate them is needed. Following the method used by Myschik et al, these angles can be estimated[56]. Several simplifications will be made to their process however. Since aircraft in general, but especially sailplanes are flown at very small (ideally zero) side slip, we can assume that any lateral acceleration is the result of disturbances and not application of the aircraft controls. Given an aerodynamic model for the aircraft, the side slip angle can then be estimated through the side slip to lateral force coefficient $-C_{y-\beta}$.

$$\beta \approx \frac{ma_y}{\bar{q}SC_{y-\beta}} \quad (2.20)$$

The significant contributors to lift force are more diverse than to side force, so arriving at a good estimate of angle of attack is more challenging. Using a similar form to Equation 2.20, the angle of attack can be estimated from the dominant terms in a linear expansion of the stability derivatives, though less complete than that used by Myschik.

$$\alpha \approx -\frac{ma_z}{\bar{q}SC_{L-\alpha}} - \frac{C_{L0}}{C_{L-\alpha}} \quad (2.21)$$

Since a significant number of terms are neglected here, it bears a formal treatment of the error introduced into the wind measurement through this approximation. Computing the Jacobian of Equation 2.21

$$\begin{bmatrix} \frac{\partial \alpha}{\partial a_z} \\ \frac{\partial \alpha}{\partial V} \\ \frac{\partial \alpha}{\partial C_{L-\alpha}} \\ \frac{\partial \alpha}{\partial C_{L0}} \end{bmatrix} = \begin{bmatrix} \frac{2m}{\rho SV^2 C_{L-\alpha}} \\ \frac{-ma_z}{\rho SV^3 C_{L-\alpha}} \\ \frac{-2ma_z}{\rho SV^2 C_{L-\alpha}^2} - \frac{C_{L0}}{C_{L-\alpha}} \\ \frac{-1}{C_{L-\alpha}} \end{bmatrix} \quad (2.22)$$

Considering the magnitudes of the neglected terms in Equation 2.21, several of the largest are considered $-C_{L-q}$, $C_{L-\dot{\alpha}}$, and $C_{L-\delta_e}$ these are then dimensionalized by conservatively large values of their stability variable.

| | Derivative | Multiplier | C_L Contribution |
|----------------------|------------|------------|--------------------|
| $C_{L-\dot{q}}$ | 9.9 | 0.0089 | 0.0880 |
| $C_{L-\dot{\alpha}}$ | 3 | 0.0089 | 0.0267 |
| $C_{L-\delta_e}$ | 0.3037 | 0.5236 | 0.1590 |
| Σ | | | 0.2737 |

Table 2.2. Contributions of Largest Unmodeled Terms in Linear C_L Model to Estimated Angle of Attack

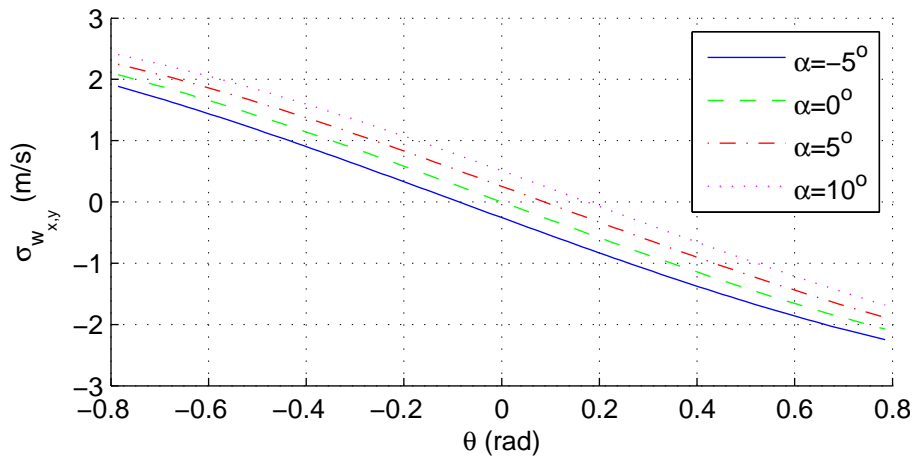
| | |
|-------------------------|--------------------|
| σ_{a_z} | 1 m/s ² |
| σ_V | 1 m/s |
| $\sigma_{C_{L-\alpha}}$ | 0.5 |
| $\sigma_{C_{L0}}$ | 0.2737 |

Table 2.3. Uncertainty in the contributors to angle of attack estimation error

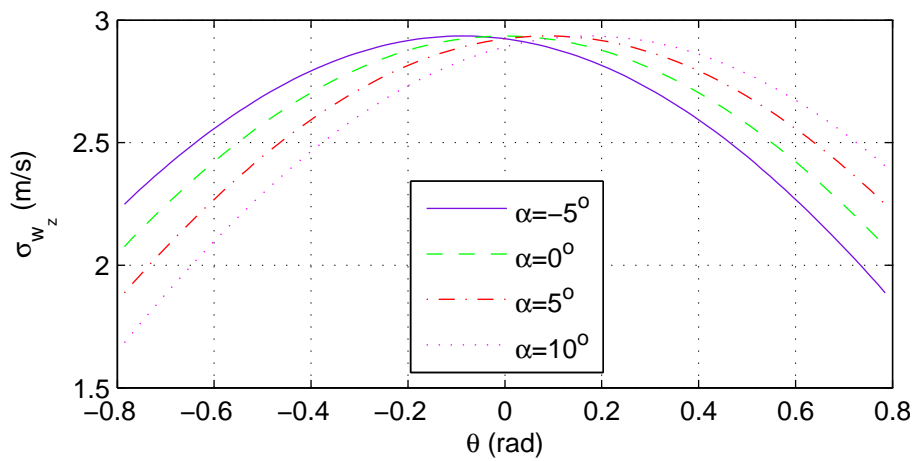
The magnitudes of q , $\dot{\alpha}$, and δ_e corresponding are $\pi/2$ rad/s, and 15° . This uncertainty is placed into that of zero angle of attack lift coefficient, with an additional 0.1 for the uncertainty in C_{L0} itself. A summary of the remaining uncertainties needed to evaluate equation Equation 2.22 are provided in Table 2.3.

A representative flight condition of $V_a = 20\text{m/s}$ and $a_z = 20\text{m/s}^2$ was chosen, giving $\sigma_\alpha = 0.1957$ rad. The resulting uncertainty in vertical and horizontal winds was computed for a range of pitch angles and angles of attack. The uncertainty is depicted in Figure 2.9.

A greater uncertainty is seen in the updraft velocity than the horizontal wind for small pitch angles. The uncertainty in the vertical velocity is compounded by the fact that it is expected to be relatively small compared to the horizontal wind speed. For static soaring, this presents a serious problem as vertical velocity is of prime importance. The greater updraft uncertainty is mitigated however as static soaring techniques are more concerned with the net vertical velocity of the aircraft (rather than the air mass motion itself), and because the use of a total energy variometer allows the energy rate of the sailplane to be directly measured.



(a) Horizontal.



(b) Vertical.

Figure 2.9. Uncertainty in the wind measurements as a function of pitch angle for several angles of attack.

Wind Mapping

3.1 Kalman Filters, Estimation, and Wind Mapping

Viewing the atmosphere as a dynamic system, then any representation of the wind structure can be considered simply as an expression of the underlying atmospheric state. Different methods of modeling the wind can be thought of as a coordinate transformation in the atmospheric state. This idea is very powerful and underpins modern data assimilation methods used to combine atmospheric observations with numerical weather prediction models[57].

In the more restricted case of determining atmospheric wind structure surrounding an air vehicle, the dynamical system view is equally useful. As a dynamical system, conventional engineering methods to estimate the state of a system can be used, in particular the Kalman filter and its nonlinear extensions. In its simplest form, the Kalman filter provides the optimal, unbiased estimate of the state of a linear system subject to Gaussian random process and measurement noise[58]. Extensions to the Kalman filter allow non-linear systems to be treated, and while they no longer can claim optimality, experience shows the estimates produced to be very good[58, 59].

3.2 Mapping an *a priori* Determined Structure

If the shear structure is known *a priori* to have a structure which can be defined parametrically, then the estimation problem is reduced simply to a parameter estimation problem – determining the static (or slowly time-varying) parameters of the wind model.

3.2.1 Variability of the Mean Wind Field

When modeling pre-determined structures, the parameters defining the wind field shape are treated as slowly varying constants. The validity of this approach bears some consideration for shears of interest to dynamic soaring.

3.2.1.1 Boundary Layer Shear

Considering the diabatic wind profile in the boundary layer[60]:

$$u = \frac{u_*}{\kappa} \left[\ln \frac{z}{z_0} + f(z, z_0, \mathcal{L}) \right] \quad (3.1)$$

Where $u_* = \sqrt{(\overline{w' u'})_0}$, the surface momentum flux and \mathcal{L} is the Monin-Obukhov parameter[60]:

$$\mathcal{L} = -\frac{u_*^3 \bar{\theta}_v}{\kappa g (\overline{w' \theta'_v})_0} \quad (3.2)$$

With θ_v the boundary layer virtual potential temperature, κ the von Kármán constant and $(\overline{w' \theta'_v})_0$ is the surface buoyance flux. The wind profile is a function of:

- Surface momentum flux, a function of the outer flow velocity, determined in the mean by synoptic and mesoscale forcing.
- Mean boundary layer temperature, determined by the synoptic temperature structure and diurnal heating.
- Surface buoyancy flux, a function of the stability and diurnal heating.
- Roughness length, a characterisic of the local terrain.

Restricting our consideration to homogenous terrain as complex terrain is unsuitable for boundary layer dynamic soaring due to the difficulty of assuring terrain separation (not to mention that complex terrain is likely to support other sources of shear or vertical velocity), then the boundary layer parameters are all functions of synoptic or mesoscale forcing and diurnal heating. In the absence of discontinuous features such as cold fronts (which are likely to support static soaring as an alternative), the boundary layer wind profile will then be relatively stable on time scales between several minutes and several hours. Indeed this is borne out by Van der Hoven's study of the spectrum of atmospheric motion[1], reproduced in Figure 3.1.

Convective boundary layers do complicate matter somewhat, as their contribution to wind variation occurs with a period of several minutes (the second peak in Van der Hoven's spectrum. As with fronts, a convective boundary layer supports static soaring, providing greater terrain clearance and vision range for an aircraft, consequently here it is supposed that dynamic soaring would only be preferred when no other soaring techniques are available. Considering stable boundary layers, fluctuations about the mean shear structure can then be interpreted as random turbulence after the Dryden model[53]. The slow variations of the mean profile can then be tracked by appropriate selection of the Kalman filter process noise.

3.2.1.2 Ridge Shear

The approach taken for boundary layers is not applicable to ridge shears, as the separated region is driven by turbulent motion and a non-hydrostatic pressure gradient. Intermittent separation

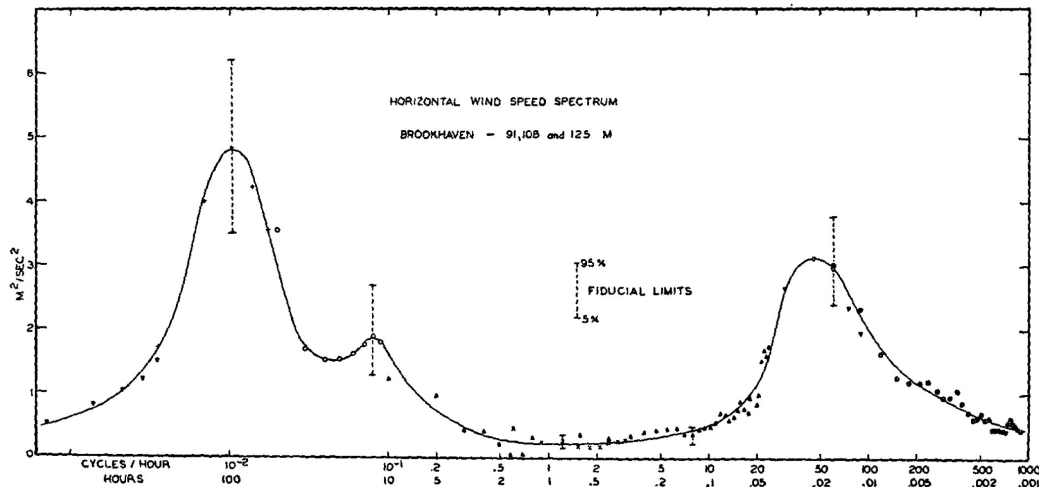


Figure 3.1. Power spectrum of horizontal winds, measured at Brookhaven National Laboratory. Reproduced from "Power Spectrum of Horizontal Wind Speed in the Frequency Range from 0.0007 to 900 Cycles per Hour"[1]

as vortices are shed further complicates the picture[61]. Considering the separated region in the mean sense however, Wood presents a metric for the onset of separation from hills based on the wavelength and surface roughness length[62]. If the intermittent character of the separation is either fast enough to be considered noise, or slow enough to appear a slow variation in the shear structure, then the mean structure can be tracked by a Kalman filter. Before attempting a dynamic soaring experiment in the lee of a ridge, further investigation of the time-varying shear structure should be undertaken.

3.2.2 Modeling Wind Profiles With the Kalman Filter

The nonlinear form of wind profile parameterizations such as power laws and log models requires use of a nonlinear filter[60, 63, 64]. Using an Unscented Kalman Filter, a set of sigma points are deterministically selected surrounding the current state estimate that captures the mean and first moment of the state probability distribution[58]. These sigma points are then propagated through the state transition model and reassembled into the mean and covariance of the state. For a randomly walking wind model, there is no state transition so the update step only requires incrementing the state covariance by a process noise selected to represent the expected maximum rate of change in the state.

When a measurement becomes available a new set of sigma points are drawn with the updated covariance and propagated through the measurement model to compute innovations. These innovations are then used to compute a Kalman gain matrix, update the sigma points, after which the state and covariance is recovered[58].

3.3 Mapping Arbitrary Wind Structures

A pre-specified structure is acceptable for some wind environments and has the strength of allowing a structure to be selected intelligently that captures the essential features of the expected field. In many cases however, the wind structure is chaotic and a more general solution is needed. Langelaan et al.[49] attempted to model wind shears with polynomial functions. Such functions demonstrate some skill, but attaining a sufficiently descriptive model without overfitting is challenging for polynomials. The use of piecewise polynomial splines offers an attractive alternative to polynomials, allowing complex structures to be represented compactly while reducing the overfitting seen in high-order polynomials.

3.3.1 Spline Mathematics

At its simplest, a spline is a piecewise polynomial function, and it can be constructed by piecewise summation of polynomial functions. The nature of a spline can be visualized by dividing the domain of a function into a set of segments separated by “knots” – points where the k th derivative of the function is allowed to be discontinuous, with k determining the order of the spline. Owing to its piecewise nature a spline can be written as a linear combination of simpler functions given a suitable basis. This form is known as the basis spline (or B-spline) form, and allows the spline function to be written as a linear mapping[65]:

$$\mathcal{S}(h) = \sum_{i=-k}^g c_i N_i(h) \quad (3.3)$$

Where N defines a spline basis supported on the interval defined by knots $\lambda_j, j = 0 \dots, g + 1$ and forms a partition of unity at every point $x, \lambda_0 \leq x \leq \lambda_{g+1}$. The coefficients, c are the coordinates specifying a particular function as a linear combination of the basis N . After defining the spline order and knot locations, the value of the spline basis, N , can be determined using a triangular scheme[65] described in Algorithm 1. The basis spline as a linear combination of simpler functions is depicted in Figure 3.2.

The concept of a spline can be generalized to more dimensions through use of the tensor product. In the tensor product spline, knot intervals are defined along each coordinate direction and the domain is then divided into cells defined by the Cartesian product of the knot intervals. In two dimensions this forms a rectangular mesh, with x and y knot intervals as illustrated in Figure 3.6. The spline may be represented on each rectangle by the direct product of two polynomials, one along each coordinate direction[65]:

$$\mathcal{S}_{R_{i,j}} \in \mathcal{P}_k \otimes \mathcal{P}_l \quad (3.4)$$

If $\mathcal{P}_k(x)$ and $\mathcal{P}_l(y)$ are written as basis splines as in equation 3.3, then the resulting bivariate spline can be written as the tensor product of the two spline functions, which can be written[65]:

Data: interior knots, $\lambda_{1\dots n}$; boundary knots, $\lambda_{1-k\dots 0, n+1\dots n+k}$; order, k ; point, x
Result: basis for spline at point x , $N(x)$
initialization - append boundary knots to interior knots to form full knot vector, λ^*
for $i = (n - 1) : -1 : (1 - k)$ **do**
 if $x \in [\lambda_i^*, \lambda_{i+1}^*)$ **then**
 | $E_{i,1} = 1$
 else
 | $E_{i,1} = 0$
 end
 for $j = 2 : (k + 1)$ **do**
 | $\Delta_1 = \frac{x - \lambda_i^*}{\lambda_{i+j-1}^* - \lambda_i^*}$
 | $\Delta_2 = \frac{\lambda_{i+j}^* - x}{\lambda_{i+j}^* - \lambda_{i+1}^*}$
 | **if** $\text{undefined}(\Delta.)$ **then**
 | $\Delta. = 0$
 | **end**
 | $E_{i,j+1} = \Delta_1 E_{i,j} + \Delta_2 E_{i+1,j}$
 end
 if $\lambda_i^* = \dots = \lambda_{i+k}^* < \lambda_{i+k+1}^*$ **then**
 | **if** $x \in [\lambda_i^*, \lambda_{i+k+1}^*]$ **then**
 | $E_{i,k+1} = \left(\frac{\lambda_{i+k+1}^* - x}{\lambda_{i+k+1}^* - \lambda_i^*} \right)^k$
 | **else**
 | $E_{i,k+1} = 0$
 | **end**
 end
 if $\lambda_i^* < \lambda_{i+1}^* = \dots = \lambda_{i+k+1}^*$ **then**
 | **if** $x \in [\lambda_i^*, \lambda_{i+k+1}^*]$ **then**
 | $E_{i,k+1} = \left(\frac{x - \lambda_i^*}{\lambda_{i+k+1}^* - \lambda_i^*} \right)^k$
 | **else**
 | $E_{i,k+1} = 0$
 | **end**
 end
end
 $N = E_{1:(n+k-1), k+1}$

Algorithm 1: B-spline computation algorithm.

$$\mathcal{S}(x, y) = \sum_{i=-k}^g \sum_{j=-l}^h c_{i,j} N_i(x) M_j(y) \quad (3.5)$$

With knots λ_i in x and μ_j in y fixing N and M , the values $c_{i,j}$ will define the shape of the spline function. The bilinearity of the tensor product[66] ensures that the final spline function is linear, thus $c_{i,j}$ can be estimated using any linear estimation procedure.

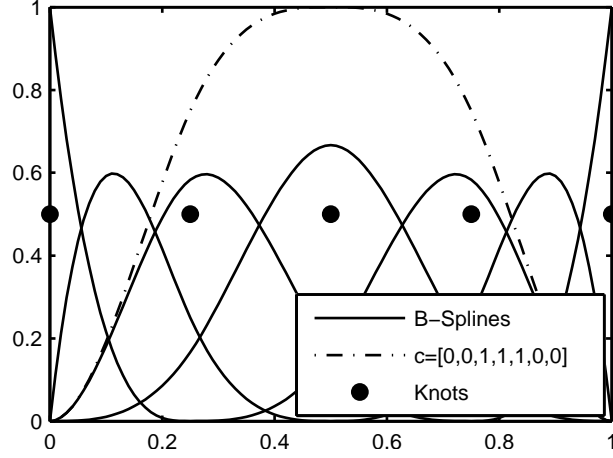


Figure 3.2. Basis splines and one example spline with knots $[0, 0.25, 0.5, 0.75, 1]$, order 3

3.3.2 Wind Mapping with Splines

Since the spline $\mathcal{S}(z)$ represents a linear mapping, it can be implemented in a Kalman filter to build a model of the wind environment as measurements of the wind field are taken. The Kalman filter states form a vector concatenating the spline coordinates in each direction:

$$\mathbf{X} = \begin{bmatrix} \mathbf{c}_{north} \\ \mathbf{c}_{east} \\ \mathbf{c}_{down} \end{bmatrix} \quad (3.6)$$

If a model is available for the time evolution of the wind field, it can be used to propagate the spline coefficients forward in time. Assuming here, that changes in the wind field are small and random so that the state transition is trivial, the Kalman filter can be constructed with the prediction step proceeding:

$$\begin{aligned} \hat{\mathbf{X}}_{t|t-1} &= \hat{\mathbf{X}}_{t-1|t-1} \\ \hat{\mathbf{P}}_{t|t} &= \hat{\mathbf{P}}_{t|t-1} + \mathbf{Q}_t \end{aligned} \quad (3.7)$$

Since the spline coefficients form a linear mapping and the basis a partition of unity[65], a uniform bias in the coefficients will result in an identical bias in the wind model for any point in the wind field. This property of the basis spline offers a convenient way to select a process noise with physical meaning – the process noise is chosen to be the expected uniform change in the wind field between iterations of the Kalman filter, allowing it to “walk” with time.

The observation model is defined as a block diagonal of the spline basis at the current aircraft location:

$$\mathbf{H}_t = \begin{bmatrix} \mathbf{N}_{north}(h) & 0 & 0 \\ 0 & \mathbf{N}_{east}(h) & 0 \\ 0 & 0 & \mathbf{N}_{down}(h) \end{bmatrix} \quad (3.8)$$

Where $\mathbf{N}_{(\cdot)}(h)$ is a row-vector defining the spline basis at the current aircraft location. While the state and observation model structures described here permit different spline models to be used for each coordinate direction, the use of identical spline bases is advantageous from a computational perspective as the spline basis must only be evaluated once per measurement update.

The remainder of the Kalman filter proceeds conventionally:

$$\begin{aligned}\mathbf{K}_t &= \hat{\mathbf{P}}_{t|t-1} \mathbf{H}_t^T (\mathbf{H}_t \hat{\mathbf{P}}_{t|t-1} \mathbf{H}_t^T + \mathbf{R}_t)^{-1} \\ \hat{\mathbf{X}}_t &= \hat{\mathbf{X}}_{t|t-1} + \mathbf{K}_t (\mathbf{w} - \mathbf{H}_t \hat{\mathbf{X}}_{t|t-1}) \\ \hat{\mathbf{P}}_{t|t} &= (\mathbf{I} - \mathbf{K}_t \mathbf{H}_t) \hat{\mathbf{P}}_{t|t-1}\end{aligned}\tag{3.9}$$

The wind measurement covariance, \mathbf{R} and measured wind velocity, \mathbf{w} , are determined by comparing the air and inertial velocity vectors[55, 56, 67]. Even with an arbitrarily detailed spline model (unrestricted in the number of coefficients required to define the model), the quantity $(\mathbf{H}_t \hat{\mathbf{P}}_{t|t-t} \mathbf{H}_t^T + \mathbf{R}_t)$ reduces to a 3×3 matrix, so the filter runs very rapidly.

While the filter is developed here in north/east/down coordinates, any three-component system could be used to model the three-dimensional wind field. While modeling in cylindrical coordinates has been previously demonstrated[49], and offers natural intuition in the way we typically think of wind (ie. speed and direction), the wind estimation algorithm used naturally develops wind in Cartesian coordinates. Conversion to cylindrical coordinates can introduce a non-linearity if one of the wind components fluctuates around zero as both positive and negative wind components contribute to the magnitude estimate.

3.4 Combined Model and Model-Free Wind Mapping

Despite the flexibility of spline models, they retain some of the problems of polynomials as modeling functions. One of the challenges they face is modeling the strong curvature found in the lower part of a boundary layer or in a sigmoid-shear. If significant detail is desired in one of these strongly curved regions, a combined modeling technique can be adopted, using splines to model the gross characteristics of the wind field while a prescribed model captures the fine details. In wind field estimation for ridge dynamic soaring, this approach is adopted to find the strength and vertical position of the shear while splines are used to determine the direction of the shear and to provide a check on the model’s sanity.

The wind direction can be determined from the spline model by using a principal component analysis of the matrix formed by multiplying the north and east spline model coefficients.

$$\mathbf{M} = \mathbf{c}_e^T \mathbf{c}_n\tag{3.10}$$

Using singular value decomposition a diagonal matrix component can be extracted, and the arctangent of the leading two components used to determine an “effective direction” for the layer in question.

This technique has the advantage of capturing the direction influence of every layer in the shear and weighting it appropriately by the wind strength. If a simple low-pass filter is instead used on the instantaneously measured direction, then the noisy signal in the low-wind section would impact the wind direction equally to the strong wind above the shear, which is more important when planning DS paths.

3.5 1-D Mapping Results

The combined modeling method was applied in both simulation and flight tests to test its ability to map the wind field. Validating a wind model in flight is challenging as high-resolution observational data is unavailable. A combination of simulation and flights is thus used to establish the basic validity of the modeling technique.

3.5.1 Simulations

3.5.2 Fox Boundary-Layer Data

During a flight test of the E-Scale Fox, data was recorded at 25Hz from the Piccolo autopilot and used to drive a boundary-layer modeling wind map. For safety of flight, the aircraft was not flown in the lower boundary layer so no data was gathered below 40m where the wind profile exhibits the most curvature. A boundary layer structure is still observed however, the profile estimated from the spline model is depicted in Figure 3.3.

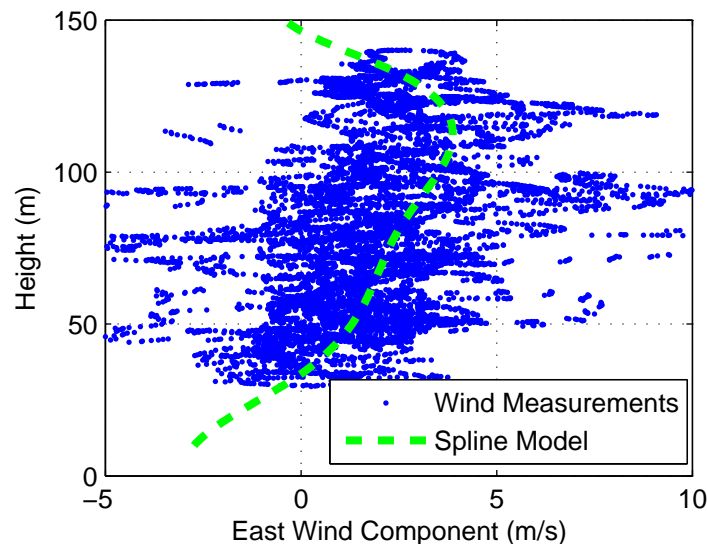


Figure 3.3. Spline and parameter fit to boundary layer winds estimated from flight data during 18 Jan flight test. The aircraft was under manual control so the flight path was highly erratic, contributing to the noise seen in the wind measurements

3.5.3 Ridge Shear Modeling Simulation

To test the combined model and model free approach, a simulation of an aircraft dynamic soaring behind a ridge is used. The simulation is implemented in MATLAB using the equations of motion developed in Section 2.2.2 and the aircraft performance model from Section 2.2.3. The aircraft is initialized at the surface, climbs to intercept a shear at $h=100$ m and then begins dynamic soaring. Since the intent here is to test the wind mapper in dynamic soaring, the controller is given the wind profile *a priori* and in addition to the controller discussed in Section 5.4 it is equipped with direct thrust and C_L control to ensure it flies the proper dynamic soaring path.

A 500 run Monte Carlo simulation is used to diagnose the reliability of the wind mapping method. The wind map is initialized with the shear bottom at 95 m, a thickness of 30 m, and a shear strength of 8 m/s. Environmental conditions locate the shear at $h=100$ m, a thickness of 5 m, and strength of 6 m/s. Process noise is set in the Kalman filters to allow the shear to drift by 1 m/s in magnitude and 1 m of location and thickness per 100 seconds. The simulations were conducted with Dryden turbulence of random amplitude with a mean 20 foot wind parameter of 9 m/s and standard deviation of 3 m/s.

Figure 3.4 illustrates the convergence of the wind field estimate for the average of all runs. Steady-state error is visible in both the magnitude and location estimates. The true shear parameters lie outside of even three standard deviations of the Monte Carlo simulation results. This is possibly due to the nonlinear nature of the function to be estimated – nonlinear Kalman filters can introduce steady-state error for nonlinear systems.

Another source of error however, is the simulation time step. Examination of the wind profile produced by the simulation (the actual simulation aircraft and wind state) shows that the very sharp shear combined with an insufficiently fine time step produces hysteresis in the simulation wind profile as illustrated in Figure 3.5. While a finer time step does improve the simulation hysteresis, the wind map error remains roughly the same. The estimated shear is however, thicker than the true shear so a trajectory selected using the wind map for guidance will have a surplus of energy. Examining the estimated error (based on the state covariance of the Kalman filter) and comparing it to the scatter in the simulation output, the uncertainty in the shear state is clearly underestimated.

These results make it clear that estimating the parameters of a very sharp shear is challenging, and raise questions about the viability of a dynamic soaring system if very accurate shear estimation is required. Clearly, further investigation of the wind estimation requirements of a dynamic soaring system is needed. For this reason, HiL simulations are used to investigate in further detail the operation of the dynamic soaring system, where trajectories will be planned using the wind map output and the aircraft will attempt to fly them. HiL simulation is discussed in Section 5.6.

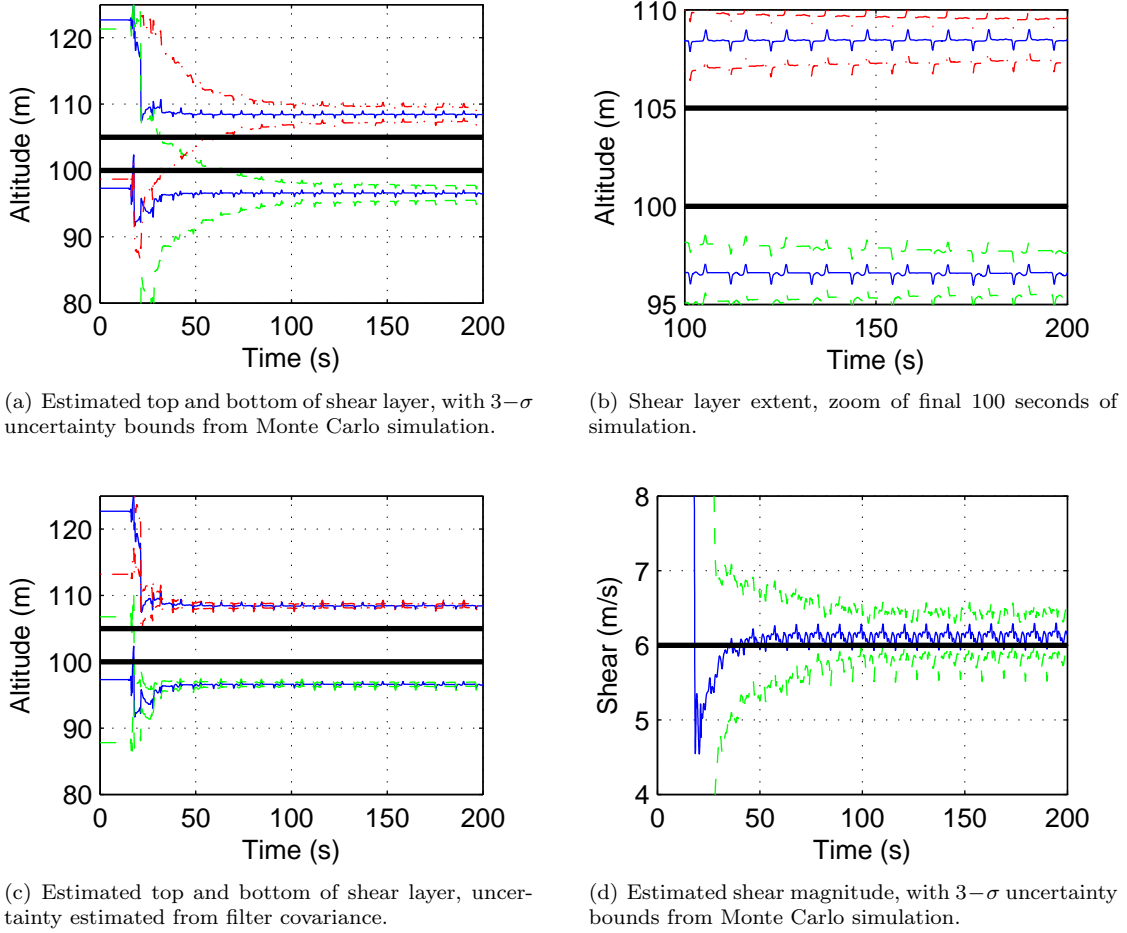


Figure 3.4. Wind map estimates and $3-\sigma$ confidence bounds for a 500 run Monte Carlo simulation series. Each run flies the same trajectory and is seeded with a random turbulence value of mean $\bar{U}_{20} = 9$ m/s and covariance of 3 m/s. All simulations are run with a shear of 6 m/s located between 100 m and 105 m, the true shear is indicated with thick lines.

3.6 Mapping Multi-Dimensional Wind Structures

By extending the spline model into another dimension via the tensor product spline, it can be used to model wind structures in higher dimensions. The tensor product spline, Equation 3.5, shows that linearity is preserved in this operation so the Kalman filter can again be easily applied, with just an increase in the number of states. While the 1-D spline has $n + k - 1$ states where n is the number of knots and k the order, the 2-D spline has $(n + k - 1)(m + l - 1)$ states. This is manageable however, as the matrix inversion in the Kalman filter update reduces to a single value if a direct measurement of a wind component is available (as measured from a variometer for example), or a 3×3 matrix to account for correlation of wind components if the vector wind computation is used. Figure 3.6 illustrates an example 2-D spline analogous to Figure 3.2.

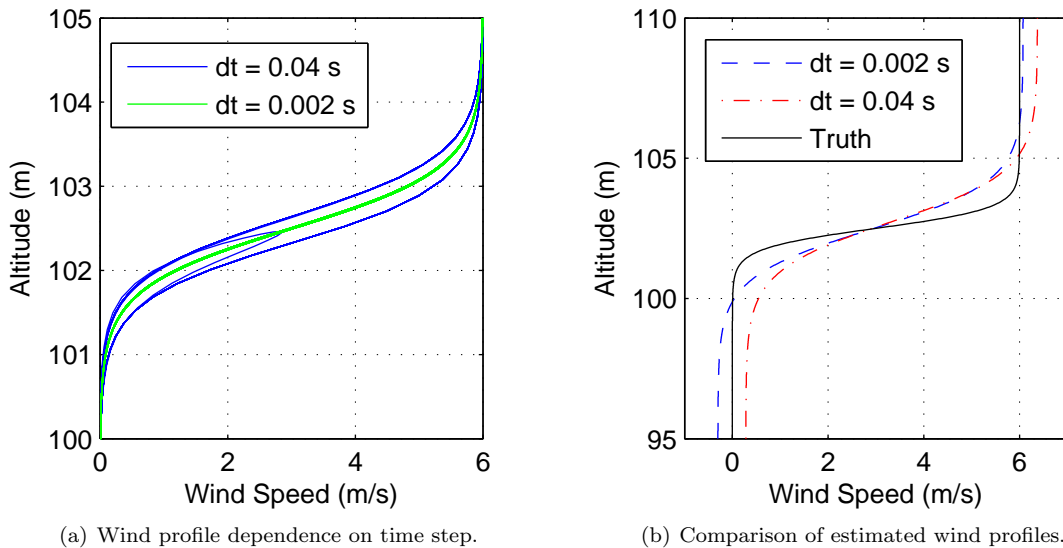


Figure 3.5. Wind profile dependence on simulation time step size, the very sharp shear creates numeric difficulties as the aircraft crosses the shear layer.

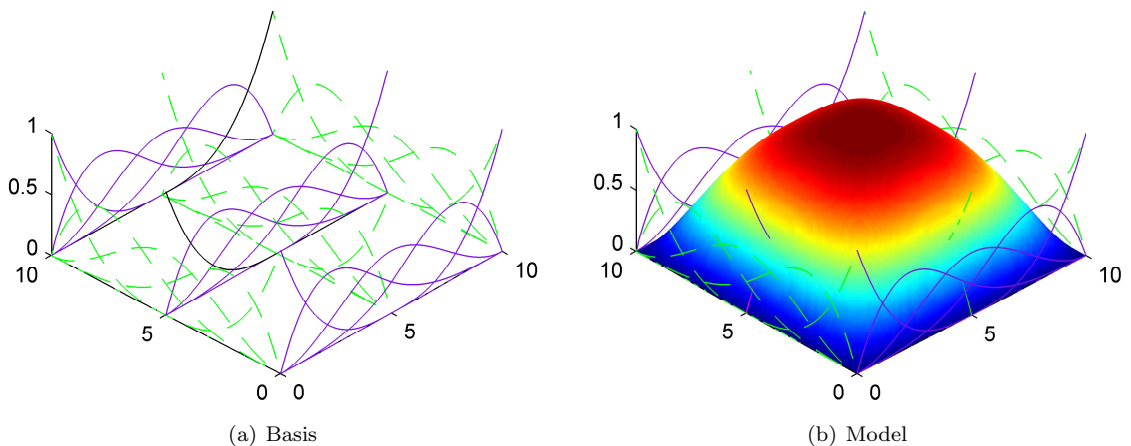


Figure 3.6. Basis and a representative 2-dimensional tensor product spline. In this case knot distribution is uniform and identical in each direction, but this is not necessary.

3.6.1 Thermal Simulation Results

A number of thermals were randomly generated and an encounter between an aircraft and the thermal simulated using the equations of motion presented in Section 2.2.1. Both type 1 and type 2 thermals were simulated 160 times each with a mean strength of 2 m/s and standard deviation of 1 m/s, updraft measurements were corrupted with zero mean Gaussian noise with standard deviation 0.5 m/s. Table 3.1 shows the mean error and standard deviation in estimated core strength for both thermal types. Figure 3.7 presents the evolution of the estimated thermal structure for a type 2 thermal. The region where the outer ring is missing in the model is an area where the aircraft did not fly (and thus had no information about the thermal structure).

| | Mean Core Strength Error | Core Strength Error Standard Deviation | Runs |
|--------|--------------------------|--|------|
| Type 1 | 0.8% | 0.21 m/s | 124 |
| Type 2 | -6.6% | 0.34 m/s | 128 |

Table 3.1. 2-D spline modeling errors from Monte-Carlo simulations. Each thermal type was simulated in 160 trials, some runs were excluded because the thermal core was very weak (less than 1 m/s) or because the aircraft failed to intercept the thermal.

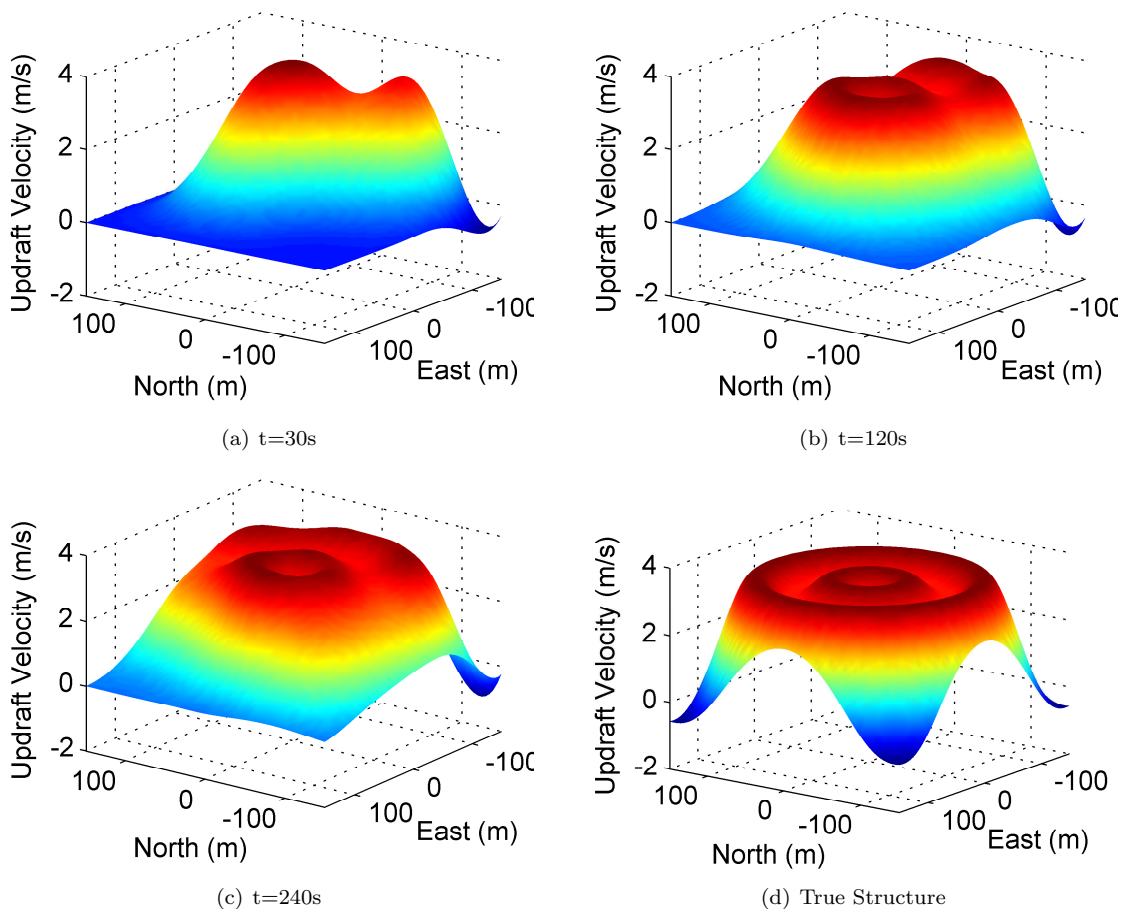


Figure 3.7. Evolution of the thermal map for a type 2 thermal $w_0 = 4.4$ m/s, $C = 42.93$ m. Breaks in the outer ring are in regions not sampled by the sailplane.

Optimizing Thermal Soaring

Conceptually, the advantage of modeling the local wind environment could dramatically improve the performance of thermal centering controllers. Naive controllers, assuming an axisymmetric thermal stand at odds with observations of glider pilots that “lift is where you find it,” belying the complex structure of most real thermals. The existence of a map is not in itself a solution however, a means of exploiting that information is required. A thermalling method is presented here that uses the thermal map to improve a sailplane’s climb rate by flying along constant-updraft contours.

4.1 Thermal Contour Paths

The Reichmann thermal method suggests turning tighter in sink and wider in lift, attempting to center the sailplane on the thermal and maintain a constant climb rate[13]. Andersson developed a soaring controller which quantifies the feedback in this algorithm, varying the turn rate until a constant turn rate is achieved with constant climb rate[16]. For an aircraft which is mapping a thermal, this idea can be taken one step further. With a map of the thermal available a path can be planned to explicitly fly along a contour of constant vertical velocity.

Planning contour paths is relatively simple, the spline model is evaluated at a number of points on a grid. The resolution must be sufficient to resolve any important features of the thermal field, extremely high resolution is not required however as the aircraft turn radius defines a limit to how fine the resolution should sensibly be. A contouring tool for gridded data is then used to compute a contour at the desired level.

Determining the optimal contour level is straightforward but slightly more computationally intensive as it must be done iteratively. A cost function is defined, giving the mean climb rate around a given contour:

$$J(w, u) = \bar{z} = \oint_{C(w)} (w - \dot{z}(u)(s)) ds \quad (4.1)$$

If the aircraft is assumed to be in steady level flight, then the sink rate, $\dot{z}(u)$, can be computed easily from the polar, speed, and turn radius. The turn radius is computed at each point on the trajectory by fitting a circular arc to the point of interest and two points each preceding and following (five points in total), allowing the load factor to be computed:

$$n = \sqrt{\left(\frac{a_c}{g}\right)^2 + 1} = \sqrt{\left(\frac{u}{gR}\right)^2 + 1} \quad (4.2)$$

The required lift coefficient can then be computed by the conventional definition, with $L = mgn$. The speed is treated as an optimization variable, constant for each contour level. The sink rate can then be computed from the drag polar:

$$\dot{z}(u) = \frac{\rho u^3 C_D(C_L) S}{2mg} \quad (4.3)$$

Where $C_D(C_L)$ indicates that the drag coefficient is computed as a function of C_L . The aircraft is “flown” around a candidate trajectory and the difference of the sink rate on each segment and contour level is integrated to compute the climb in a circuit, divided by the time required to fly a contour the mean climb rate is achieved. A nonlinear optimization routine can then be used to compute the optimal contour level and speed.

In addition to exploiting the aircraft model and the thermal map information, this approach offers a natural way to deal with complex thermal structures. To account for the effect of complex thermal geometries which have multiple cores or concave shapes along a contour, the convex hull of contours of a given level is also considered as a valid path. This allows the aircraft to consider thermals with multiple cores not large or strong enough to circle singly. Figure 4.1 illustrates the evolution of a trajectory through several iterations.

This planning method does suffer from the quandary inherent in simultaneous mapping and exploitation of any resource – insufficient mapping of the wind field potentially leaves an area unexplored which could improve climb rate, but a thorough exploration takes time which degrades average climb rate. In an attempt to balance these competing objectives, a dither is applied to the aircraft goal location’s radial distance from the path centroid. In this investigation a sinusoidally varying dither is applied with amplitude of 20 meters and period of 15 seconds. A dither amplitude based on the local uncertainty in the thermal map may deliver higher performance, but a fixed dither is used here for simplicity. This dither allows the aircraft to explore a region close to the current trajectory.

4.2 Closed-loop Control

With a path defined, a controller is needed to keep the aircraft following the desired contour. The controller used here is a high level controller, developed under the assumption that lower level control (roll angle, airspeed control, etc) is already provided for on the UAS platform. The controller implemented in this investigation is developed from the guidance method presented by

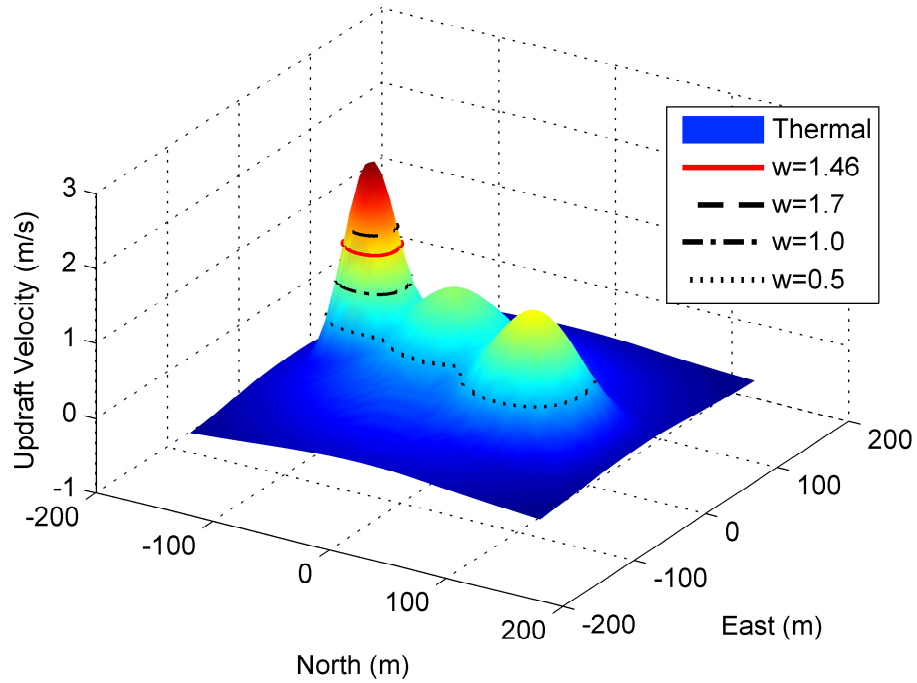


Figure 4.1. Contours at several levels, illustrating the evolution of trajectory planning at several levels. The red trajectory is optimal at an airspeed of 14.8 m/s and achieves a mean climb rate of 0.86 m/s.

Park et al[35]. They present a controller which generates a lateral acceleration command from the bearing to a reference point located on the desired path at a fixed distance from the vehicle.

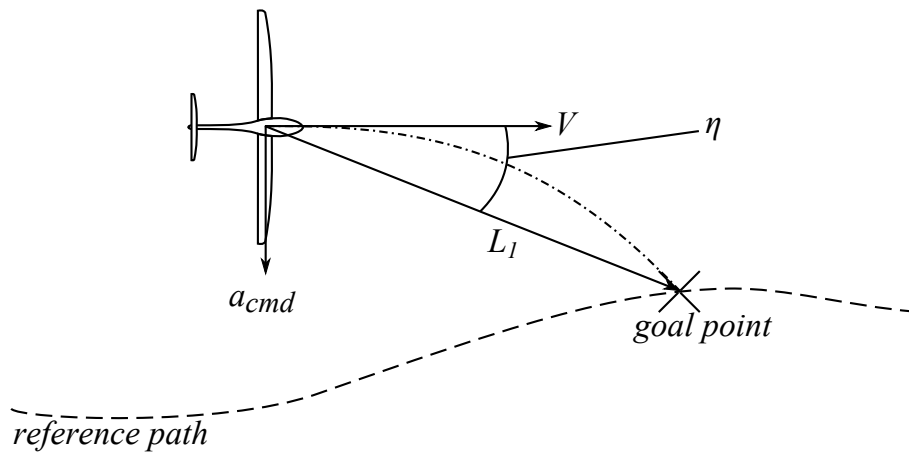


Figure 4.2. Illustration of Nonlinear guidance law from Park, et al

The goal point progresses along the reference path to always be at distance L_1 away from the aircraft. The lateral acceleration a_{cmd} is then given by:

$$a_{cmd} = 2 \frac{V_a^2}{L_1} \sin(\eta) \quad (4.4)$$

This guidance law gives good convergence and excellent tracking when compared with PID controllers[35], but presents several problems in this application. First, it cannot be guaranteed that there will be a point on the path that is distance L_1 away, especially when the contour is recalculated. Second, a closed path is more easily parameterized in polar coordinates. For these reasons, Park's guidance law is modified to use a constant look-ahead angle instead of distance. Use of the modified controller proceeds as:

1. The desired contour and aircraft position are shifted to put the path centroid at $(0, 0)$. The path and aircraft position are then transformed to polar coordinates.
2. The goal point is selected to lie on the desired contour at a look-ahead angle of 15 deg.
3. L_1 is calculated as the distance from the aircraft position to the goal point.

This modified process is pictured in figure 4.3.

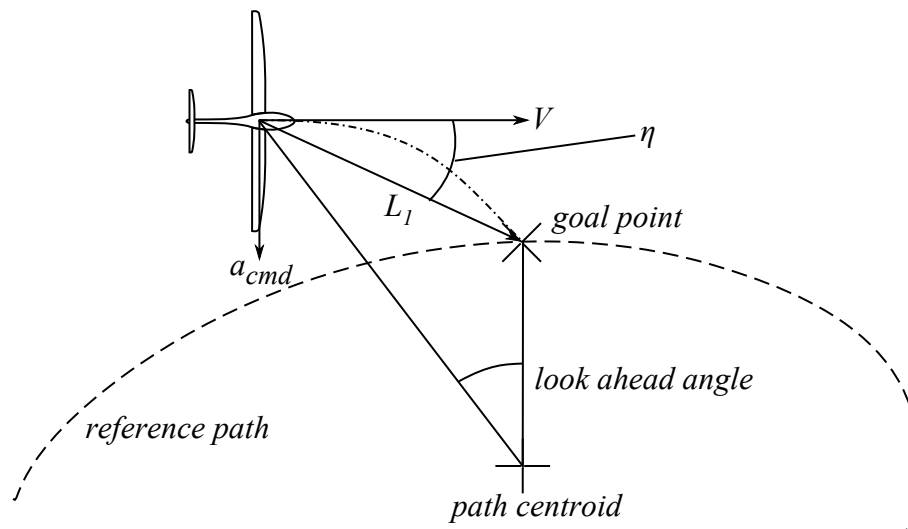


Figure 4.3. Park's Nonlinear Guidance Law Modified for Circular Trajectories

The lateral acceleration command is then calculated as in equation 4.4. This guidance method gives accurate tracking and rapid convergence for paths that are not too complicated, but can fail for paths with overly skewed dimensions or for paths that loop back on themselves, however paths of such complexity are unlikely to be encountered even in non-uniform thermals as the rapid maneuvering will increase the glider's sink rate.

4.3 Simulation Results

The thermal mapping and contour controllers were implemented in a three degree of freedom model to simulate encounters with thermals. The simulations were run for four minutes, allowing

| | Type 1 | | Type 2 | |
|----------------|--------|------------|--------|------------|
| | Mean | Covariance | Mean | Covariance |
| Strength (m/s) | 2 | 1 | 2 | 1 |
| Radius (m) | 120 | 40 | 40 | 10 |

Table 4.1. Seed values used in generating thermals. Type 2 thermal radii refer to the radius of a single core (out of four).

| | |
|----------|--------------------------------------|
| C_{D0} | 0.01 |
| m | 8 kg |
| S | 0.97 m ² |
| ρ | 1.225 $\frac{\text{kg}}{\text{m}^3}$ |
| e | 0.8 |
| AR | 17.96 |

Table 4.2. Parameters for a simplified performance model of the RnR products SBXC sailplane.

sufficient time for both the convergence characteristics and steady state performance of a controller to be evaluated. The sailplane was assumed to take a measurement of its state at 50Hz and compute a new contour path every 15 seconds.

The aircraft was initialized at one corner of a domain with the thermal at the center. The aircraft was started at a random initial heading into the domain. Thermals were of random strength and size detailed in Table 4.1.

4.3.1 Vehicle Model

The vehicle was implemented as a three degree of freedom kinematic model described in Section 2.2.1. To compute sink rate and adjust for turning performance, a glide polar was specified through a simple aerodynamic model.

$$C_D = C_{D0} + \frac{C_L^2}{\pi e AR} \quad (4.5)$$

Aircraft parameters are described in Table 4.2.

4.3.2 Simulation Results

Three thermal exploitation methods were simulated for comparison. In addition to the contour planning method, a second glider was simulated using Allen’s method[11] and a third using Andersson’s controller[16]. Figure 4.4 illustrates the flight paths flown by the three gliders during one such thermal encounter with a type 1 (single cell Gaussian) thermal.

The simulation results reveal that the planning method converges much more robustly than Allen’s method. If the initial heading of the glider only grazes the thermal, Allen’s method will often fail to intercept the thermal or intercept it on a very large circle that flies in weak lift for a considerable period before “coring” the thermal. In all simulations the thermalling controllers are always active and the aircraft is exclusively trying to thermal – there is no thermal/cruise

| Climb Rate for the Full 240 Second Simulation | | | |
|---|------------------|-------|-----------|
| | Contour Planning | Allen | Andersson |
| Min (m/s) | 0.19 | 0.23 | 0.16 |
| Max (m/s) | 3.12 | 2.87 | 3.26 |
| Mean (m/s) | 1.47 | 1.42 | 1.46 |
| Mean Climb Rate in the final 30 Seconds of Simulation | | | |
| | Contour Planning | Allen | Andersson |
| Min (m/s) | 0.28 | 0.26 | 0.25 |
| Max (m/s) | 3.47 | 3.47 | 3.65 |
| Mean (m/s) | 1.64 | 1.60 | 1.74 |

Table 4.3. Results for thermal exploitation of a type 1 thermal.

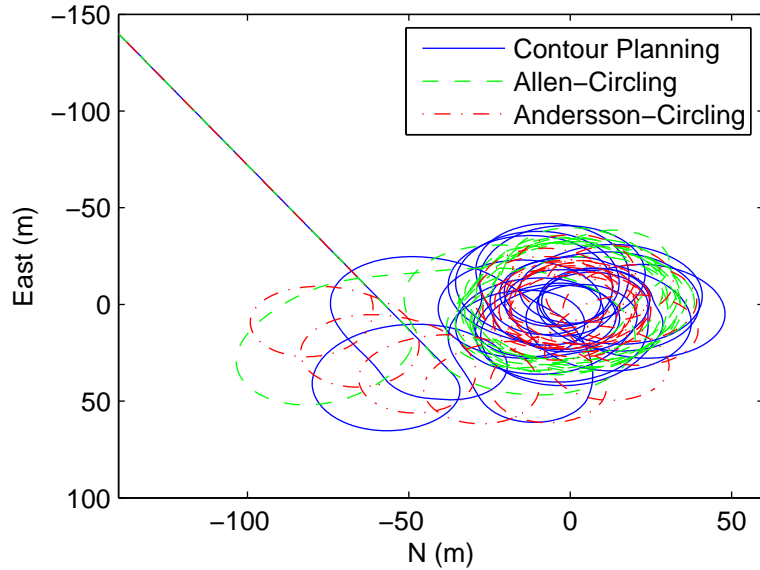


Figure 4.4. Flight paths for three thermalling techniques during a four minute simulation of an encounter with a type 1 thermal $C_0 = 3.2$ m/s, $R = 114.46$ m.

decision. Comparing the contour planner to Andersson’s controller shows a definite advantage to Andersson’s method. However, it is very sensitive to the initiation of thermalling, it was necessary to use a cruise/thermal threshold or else the Andersson-circling glider would converge extremely slowly or fail to intercept the thermal at all. Once the thermal is intercepted however, the Andersson controller exhibits robust convergence and very high climb rates, unsurprising as the single Gaussian core is exactly the thermal structure it is designed to exploit.

Restricting examination only to the cases where all aircraft successfully intercepted the thermal (approximately half of the total runs), the contour planning glider out climbed the Allen-circling glider by an average of 3.5%. Some of the climb advantage can be attributed to the reduced time required to center a thermal (under one turn in some situations). However, as Figure 4.5 shows, the final climb rate is also superior: in the final 30 seconds of simulation the contour planning method delivered climb rates 2.5% better than the Allen-circling one. Com-

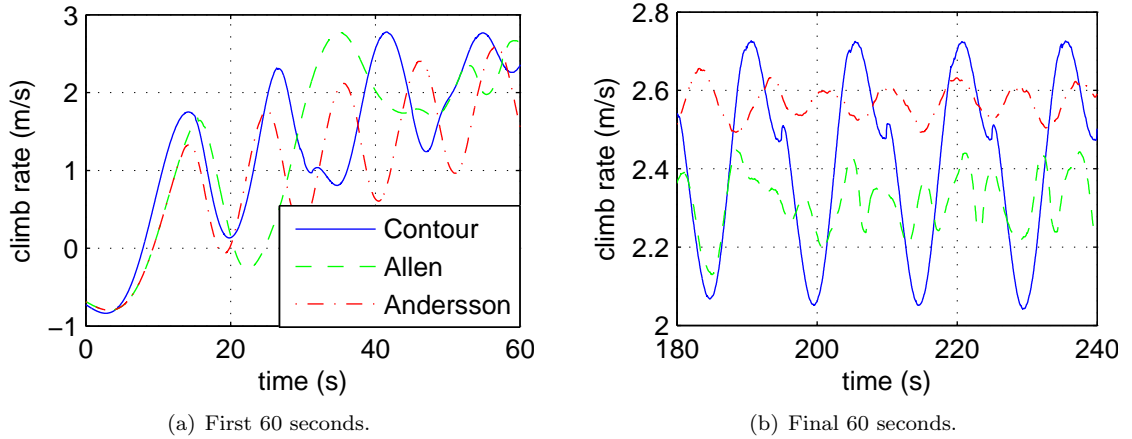


Figure 4.5. Climb rate during first and last 60 seconds of simulation in type 1 thermal. $C_0 = 3.2$ m/s, $R = 114.46$ m. The periodic notch in the planning method climb rate occurs on replanning as the aircraft maneuvers to intercept the new contour.

| Climb Rate for the Full 240 Second Simulation | | | |
|---|------------------|-------|-----------|
| | Contour Planning | Allen | Andersson |
| Min (m/s) | -0.02 | 0.06 | -0.47 |
| Max (m/s) | 4.0 | 3.46 | 3.82 |
| Mean (m/s) | 1.47 | 1.46 | 1.45 |
| Mean Climb Rate in the final 30 Seconds of Simulation | | | |
| | Contour Planning | Allen | Andersson |
| Min (m/s) | -0.02 | 0.08 | -0.44 |
| Max (m/s) | 4.16 | 3.88 | 3.92 |
| Mean (m/s) | 1.62 | 1.67 | 1.55 |

Table 4.4. Results for thermal exploitation of type 2 thermals, averaged over 160 simulations.

paring the mapping and Andersson-circling gliders, the total climb achieved is nearly identical, with the planning circling glider achieving a total climb less than 1% better on average. Comparison of the final climb rates indicates that the planning glider has an advantage in more rapid centering: despite a lower mean climb rate, the Andersson-circling glider achieved a climb rate in the final 30 seconds of simulation approximately 6% better on average than did the planning glider. Both the planning glider and Andersson-circling glider have some room to improve climb rate in the simple Gaussian thermal. The gains used for Andersson’s controller could be tuned more finely than those used here, allowing more rapid convergence. For the planning glider, a more sophisticated dithering algorithm would improve the final climb rate as the simple dithering algorithm takes the aircraft into non-optimal areas even after the thermal model has converged.

The thermalling techniques were also tested for the type 2, four cell thermal[47]. Convergence is again superior for the planning method, successfully intercepting the thermal about twice as often as Allen’s method. Examining only the converged thermals, the two methods have nearly identical mean climb rates over the course of a four minute simulation. Examining the final 30 seconds of climb shows that the steady-state climb rate is superior for the Allen-circling

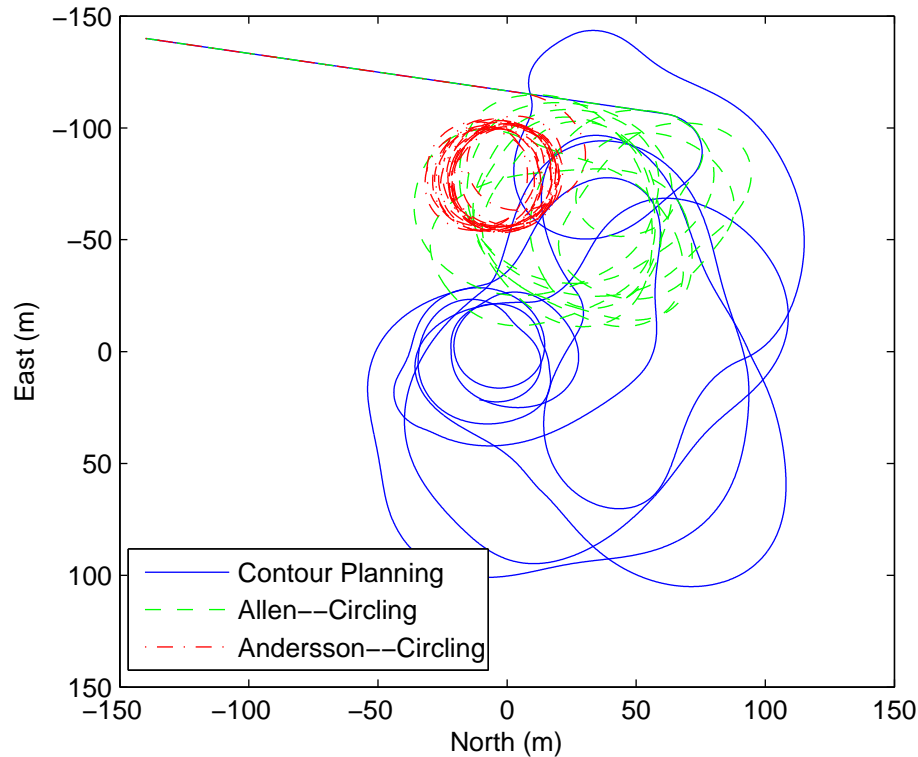


Figure 4.6. Flight paths for three thermalling techniques during a four minute simulation of an encounter with a type 2 thermal $C_0 = 4.4$ m/s, $R = 42.93$ m.

glider, with a steady state climb rate averaging 3% better than the mapping technique. The reason for the discrepancy between mean and steady-state climb rates for the four cell thermals becomes apparent when examining the flight paths in Figure 4.6. With no clear maximal point in the thermal, the contour planning glider traverses an irregular trajectory as it maps the thermal. While rapidly identifying an areas of good lift, the area is not distinct enough and the glider roams the broad region of good lift. Unlike the simple Gaussian thermal which is rapidly mapped and has a clear and easily determined structure, the complexity in the type 2 thermals occasionally leads to phantom peaks in the model. Chasing these irregularities naturally leads the planning glider to fully explore the thermal and limits the uncertainty in the model, but also degrades the mean climb rate, depicted in Figure 4.7. Table 4.4 presents the differences in climb for several simulations using the type 2 thermal structure.

Comparing the contour planning glider and the Andersson-circling glider, the mean climb rate is similar for the two techniques. The planning glider achieves a mean climb rate 1% better than the Andersson-circling glider, and in the final 30 seconds of simulation the climb rate achieved by the planning glider is 5% better than the Andersson-circling glider. The flight path trace bears this out - the Andersson-circling glider immediately starts turning in the edge of the thermal, achieving an initial climb rate advantage. Once the planning glider has sufficiently mapped the thermal it can catch up by flying a path in a more consistent portion of the thermal, seen in the

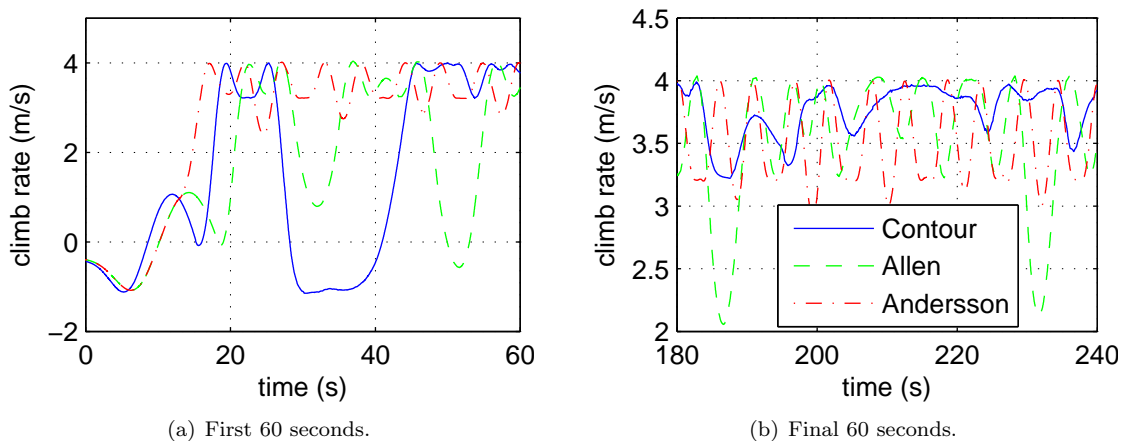


Figure 4.7. Climb rate during first and last 60 seconds of simulation in type 2 thermal. $C_0 = 4.4$ m/s, $R = 42.93$ m.

smaller variation in climb rate depicted in Figure 4.7.

The climb rates achieved by the Andersson and Allen techniques in the two thermals illustrate the sensitivity these two techniques have to assumptions built into their algorithms about thermal structure. Using the parameters specified by the authors of these controllers[11, 68], the two controllers exhibit “preferred” thermal sizes. As specified, the Andersson controller prefers a small thermal, flying tight circles which gives it good performance in the type 1 thermals with a clear and narrow core. The Allen controller prefers a larger thermal, making it better suited to centering the wide core of the type 2 thermals, where the Andersson controller is stuck on the edge and achieves a lower climb rate. The planning controller runs a course in between, delivering consistent performance in several thermal structures, though not achieving maximum climb rate in either.

Dynamic Soaring

While practiced by birds and RC sailplane pilots, dynamic soaring has thus far proved too complex for autonomous systems. As dynamic soaring is equally dependent on understanding the shear environment, planning trajectories, and controlling the vehicle, a complex system is required for its autonomous realization. Approaches taken to providing for the environmental information, decision, and control of the vehicle are presented here. A hardware in the loop simulation is used to establish the viability of the system running on available hardware.

5.1 Dynamic Soaring at Ridges

For initial investigations into dynamic soaring, the separated region in the lee of a ridge line provides an attractive environment. Very strong shear exists along the separation streamline, and has been exploited by RC pilots to fly at speeds nearing 500 mph[23]. As important as the strength of the shear is the relatively obstruction-free environment. Dynamic soaring in a boundary layer (“albatross style”) requires very precise maneuvering, as the strongest shear is closest to the surface. In the case of a ridge line, the high-energy, downward traveling portion of the dynamic soaring cycle is also taking the aircraft “downhill” so the terrain falls away from the aircraft. The increased room for maneuvering provides a more forgiving environment for initial dynamic soaring investigations.

5.2 Control Architecture

The dynamic soaring system consists of the wind mapper discussed in Section 3.4, a global planner to select the required trajectory, a local planner to fly the trajectory (described in Section 5.4), the inter-process communications structure to pass data between the components, and a communications nexus which sends and receives data from the Piccolo via a Serial connection. inter-process communications (IPC), global planner, and the Piccolo communications were

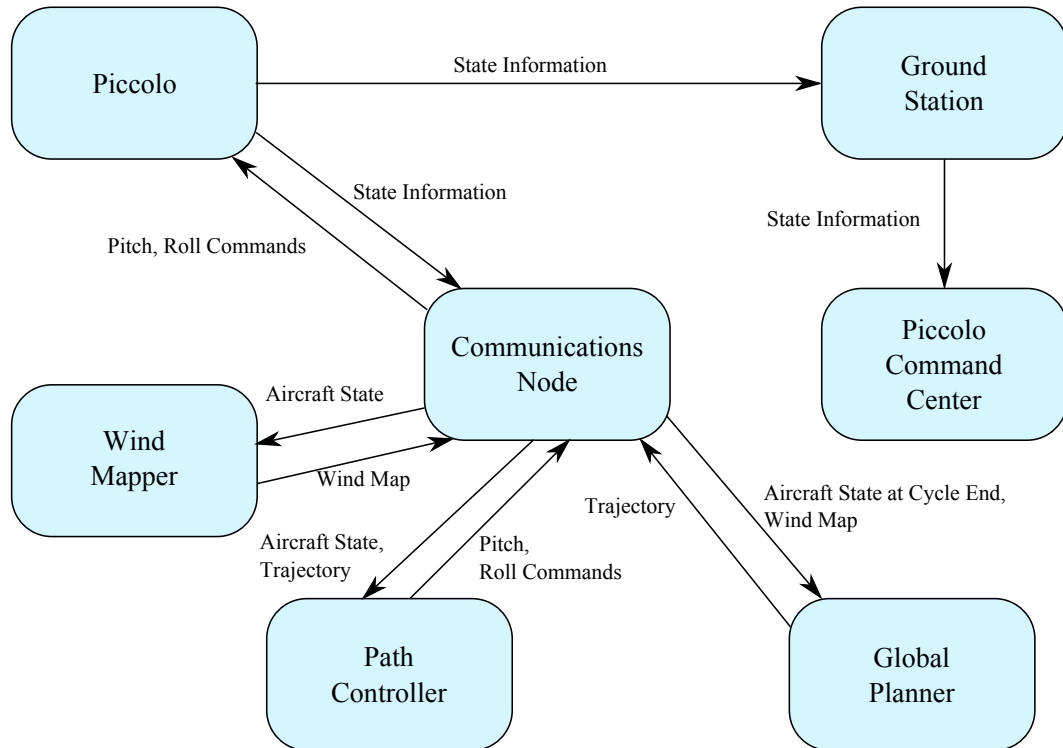


Figure 5.1. Closed loop dynamic soaring system components and communications pathways.

developed by Corey Montella at Lehigh University. The systems will be described here for completeness, Figure 5.1 shows a diagram of the system. The system is intended to run on a small single board computer on the aircraft, but for the HiL simulations presented here is run on a desktop computer.

5.2.1 Global Planner

The global planner takes the current wind field from the wind mapper, the aircraft velocity from the Piccolo, and finds a trajectory in the library that most closely matches the current conditions. This requires an extensive library of trajectories, but each trajectory requires relatively little storage and the library can be stored in an indexed form to allow rapid retrieval. The global planner monitors the aircraft location and triggers a replan when near the bottom of the DS loop, publishing the trajectory message to the other system components via the IPC software, as part of the replan the feedforward accelerations required to linearize the trajectory are computed and the path is placed relative to a pre-specified “zero” point.

5.2.2 Local Planner

The local planner subscribes to Piccolo telemetry messages and global planner trajectories. On each execution it finds the nearest waypoint and looks up the appropriate feedforward accelera-

tion, then computes the required feedback acceleration. It then computes the Piccolo commands required to achieve those accelerations and publishes them via IPC.

5.2.3 Wind Mapper

The wind mapping system uses the combined model and model-free approach discussed in Section 3.4, parameterizing the shear layer by a sigmoid model presented in Equation 2.15. It uses a linear Kalman filter with a 1-dimensional spline model to compute the wind direction, and implements the sigmoid model in an UKF to capture the details of the shear. The wind mapper subscribes to the aircraft state messages to allow it to compute the wind vector, and publishes a wind map message containing the current shear parameters – the altitude of the bottom and top of the shear, the shear magnitude, and the direction of the mean wind.

5.2.4 Piccolo Communications

The piccolo communications node forms the coordination nexus of the system, managing communications between other systems and to the vehicle itself. It subscribes to command messages, and when valid command is received it sends it to the Piccolo via serial using the Piccolo communications protocol. The communications node also monitors the Piccolo serial stream for incoming telemetry packets and publishes them to the other nodes. Testing showed that it is important to slow down the commands issued to the Piccolo. Commands faster than 25Hz will eventually slow down the Piccolo enough to trigger a reset, which is catastrophic to dynamic soaring.

5.3 Global Planning

For restricted dynamic soaring problems, such as in boundary layers or lee of ridge shears, the form of the shear can be anticipated in advance. The high-dimensionality of planning DS paths presents a formidable challenge to onboard planning in real-time, as trajectories should be updated every loop at a minimum (≈ 10 s). While adding more computational power to a small vehicle is challenging, storage is faster, smaller, and less expensive than ever. Pre-computing trajectories for all of the expected conditions and then simply retrieving the most appropriate one offers a way out of the need to plan in real-time.

The wind mapping problem is simplified in this case as well – since the form of the shear has been anticipated the mapper needs to identify parameters which bring the model most closely in agreement with observations. Use of a combined model and model free approach is ideal here – the model provides a view of the gross field and a sanity check, while the model produces the parameters required to select the proper trajectory.

5.4 Closed-loop Control

As a number of low-level control systems for aircraft exist, such as the Piccolo SL used in this investigation, closed-loop control for dynamic soaring can take a slightly higher level approach and concern itself with guiding the aircraft to a trajectory through state commands such as pitch and roll angles. The underlying autopilot system is then concerned with driving the vehicle to the desired state.

Despite this abstraction, control of a dynamic soaring aircraft presents several problems. As dynamic soaring force is dependent not just on location within the shear but on the whole aircraft state during a shear encounter, the controller must track a trajectory not just in geographic space, but in the entire aircraft state-space in order to provide adequate performance. Wind gusts, uncertainty in the shear environment, and aircraft modeling errors prevent open-loop scheduling from being an effective means of control. The rapid maneuvering required for dynamic soaring makes pure feedback ineffective as well, requiring impractically high gain in order to provide a steering command with small track errors.

To manage this challenge, a combined feedforward-feedback control architecture is used. Feeding forward commands required to fly the nominal dynamic soaring path linearizes the aircraft dynamics about the desired path. Error in the trajectory at each linearization point can then be flown out using a feedback controller with reasonable gains.

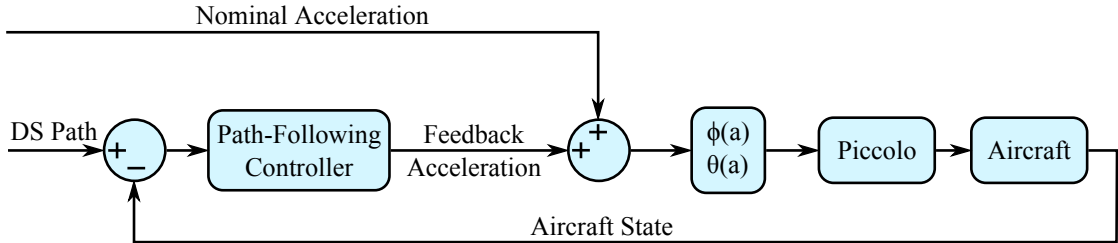


Figure 5.2. Feedforward-feedback control structure for dynamic soaring

Since the trajectory planner produces a series of aircraft states, the path is readily available as a series of “waypoints” in the aircraft state-space. At each of these points the acceleration required for an aircraft flying the path perfectly is easily computed using the dynamic soaring equations Equation 2.11. The feedforward signal is then determined by returning the nominal acceleration at the nearest waypoint. The choice of acceleration as the control is somewhat unconventional, but is readily measurable onboard the aircraft (as opposed to flight path angle, for example) and offers a natural way to fuse the feedforward with feedback commands.

The feedback signal is computed based on the error between aircraft location and the desired path. The feedback control uses the three-dimensional version of Park’s non-linear path following controller[35].

$$\mathbf{a}_{cmd} = \frac{2}{|\mathbf{L}|^2} (\mathbf{V} \times \mathbf{L}) \times \mathbf{V} \quad (5.1)$$

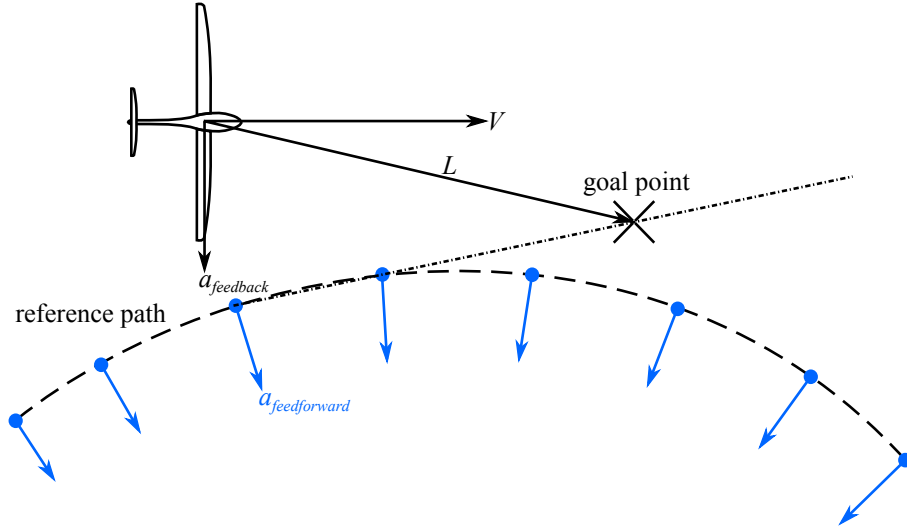


Figure 5.3. Illustration of the Geometry of the Nonlinear Guidance Law

Where \mathbf{V} is the vehicle velocity vector and \mathbf{L} a vector from the aircraft to a desired “look ahead” point on the path. The controller commands an acceleration which drives the aircraft smoothly back on the desired path.

Determining the location of the goal point can become problematic for tightly curved trajectories, if the look ahead distance is larger than the diameter of a circular path then a goal point can not be defined at all. By linearizing the trajectory about a point via the feedforward signal, the feedback controller is required only to track a straight line path tangent to the trajectory at the linearization point. This greatly simplifies computation of the look ahead and provides exactly the situation the Park controller is designed for.

Viewing the role of the feedforward as a linearization to provide the required acceleration to continue flying parallel to the path, an adjustment must be made in order to account for a difference between the aircraft radial position and desired position. If the aircraft is off the path to the “outside” – that is at a radial distance from the instantaneous center of curvature further than the nominal position – then the feedforward acceleration will be too great and the aircraft will turn toward the path. This behavior seems at first glance to be desirable, however it introduces an unexpected component to the feedback, with the feedback signal larger than expected it can introduce an oscillatory behavior to the path follower. A correction factor on the lateral acceleration is developed to eliminate this unexpected acceleration:

$$\mathbf{a}_{corr} = \mathbf{a}_{nominal} \frac{\|\mathbf{r}_{nominal} - \mathbf{r}_{centroid}\|}{\|\mathbf{r}_{aircraft} - \mathbf{r}_{centroid}\|} \quad (5.2)$$

5.5 DS Control with the Piccolo Autopilot

Since both controllers yield acceleration commands in inertial axes, they can be easily combined by simply summing into a total acceleration command. While making command composition simple, this still presents a difficulty as the lowest-level commands that the Piccolo will accept are Euler angle commands. Translating acceleration commands into a form actionable by the Piccolo is accomplished through the following process:

First, the commanded accelerations must be rotated by the heading angle into a coordinate frame with x in the direction of the flight path. Making the assumption that $\dot{\gamma} = \dot{\theta}$, desired pitch rates can then be determined through kinematics:

$$\dot{\theta} = \frac{-a_z}{V_a} \quad (5.3)$$

Observing that the lateral acceleration must come from the tilted lift vector of the banked wing, the required lateral acceleration can be expressed:

$$a_y = (a_z + g) \tan \phi \quad (5.4)$$

Which can be easily rearranged to give a bank angle which will provide the proper y to z acceleration ratio.

$$\phi = \tan^{-1}(a_y, a_z + g) \quad (5.5)$$

The achieved y acceleration will then be as commanded provided that the required z axis acceleration is achieved. Referring to the relationship between acceleration and aircraft kinematics detailed in equation 5.3, the required z acceleration can be achieved through appropriate $\dot{\theta}$. Unfortunately, $\dot{\theta}$ cannot be directly commanded to the Piccolo. The autopilot will however, attempt to achieve a first-order response to pitch angle commands. The time constant is known as it is a specified autopilot configuration parameter, so a pitch step command can be constructed to achieve the desired pitch rate.

$$\theta_{cmd} = \frac{1}{T_\theta} \dot{\theta}_{cmd} + \theta \quad (5.6)$$

As a practical consideration, it is important to note that there is no guarantee that the solution provided will be a feasible one for the autopilot to fly – for example, a sufficiently strong downward acceleration may require the aircraft to roll inverted, however the Piccolo autopilot will not allow roll angles greater than 90° . This limitation makes it critical that the trajectory generated is not only feasible for the aircraft to fly, but is not at the limits of autopilot capability in order to ensure sufficient maneuvering margin exists to fly out trajectory errors.

Another practical consideration in the implementation of this path following controller is selection of the look-ahead distance, L . This serves as a sort of convergence tuning parameter for the controller – smaller values of L lead to more rapid correction of flight path error, but can also

| | | Wind Magnitude | | |
|-----------|------|----------------|----------|----------|
| | | 6 m/s | 9 m/s | 12 m/s |
| Thickness | 5 m | 0,10 m/s | 0,10 m/s | 0,10 m/s |
| | 10 m | 0,10 m/s | 0,10 m/s | 0,10 m/s |
| | 20 m | 0,10 m/s | 0,10 m/s | 0,10 m/s |

Table 5.1. Wind and turbulence simulation conditions used to test the DS controller, the center fields indicate the 20 foot wind parameter used to seed the turbulence magnitude. To vary turbulence independently of the shear strength, the 20 foot wind is treated solely as a turbulence parameter, not as a wind speed.

destabilize the controller if L is selected too small. In simulation, the large variations in speed experienced during a dynamic soaring loop made selecting a look-ahead distance difficult as no single value provided adequate performance. A short look ahead causes the aircraft to overshoot descending portions of the trajectory and destabilize at the upper limits of the trajectory, while a long look ahead cuts off the upper portion and prevents fine trajectory control. Hand tuning revealed that specifying the look ahead as a time rather than a distance is more successful, adjusting to the significant speed variations in dynamic soaring, a value of 4 seconds provided good convergence and smooth correction of error.

5.6 Hardware-in-the-Loop Simulations

To assess the capability of the closed-loop dynamic soaring system, a series of simulation experiments were run to test the system over a range of wind conditions. While the dynamic soaring wind map and control software is run on a desktop computer, the entire Piccolo communications and control path is included in the loop. Serial communications using the Piccolo protocol is established between the dynamic soaring system and the Piccolo, and oversight is provided via the Piccolo command center which receives information via the ground station and radio link. The simulation test matrix used is shown in Table 5.1. For each run, the aircraft is started at an altitude of 0 m, with the start of the shear layer located at 100 m. The wind map is initialized with a shear location of 110 m and a thickness of 30 m, simulating a condition where forecast conditions, a pilot balloon, or prior flights have given a rough indication of the shear parameters.

The aircraft is launched and flies to a circling waypoint near the desired DS start position, it flies alternating orbits above and below the suspected shear region allowing the wind mapper to converge. Wind map convergence is assessed through the trace of the sigmoid-model covariance matrix, simulations showed that reaching a value of 0.2 consistently indicated sufficient convergence to dynamic soar. Once the wind map has converged, the aircraft is commanded to a circling trajectory tangent to a DS path. When the peak of the trajectory is the closest waypoint to the aircraft, the engine is cut and the dynamic soaring controller assumes command of the aircraft. Simulations are run for 30 minutes or until the aircraft fails to continue dynamic soaring.

5.6.1 Simulations in Smooth Air

To test the closed loop dynamic soaring system in the absence of external disturbances, a set of simulation are run without turbulence. During this initial set of simulations, the wind map convergence criterion was developed, and look-ahead time tuned for the path following controller. Table 5.2 illustrates the simulation outcomes for the shear conditions tested.

| | | Wind Magnitude | | |
|-----------|------|----------------|--------|--------------|
| | | 6 m/s | 9 m/s | 12 m/s |
| Thickness | 5 m | 30 min | 30 min | Failed to DS |
| | 10 m | 30 min | 30 min | 30 cycles |
| | 20 m | 30 min* | 20 min | Failed to DS |

Table 5.2. Dynamic soaring system performance with no turbulence. The 12 m/s condition typically failed after the Piccolo attitude filter diverged. (*–the wind map did not reach the convergence criterion before starting DS)

During this sequence of simulations, the wind mapper was discovered to under-estimate shear thickness. This was a major contributor to the diminished stability of the system in thicker shears, often the estimated thickness hovered around 15 m. Since trajectories were only available for the conditions tested, the changes would be dramatic as the planner switched between trajectories for 10 m and 20 m thick shears. Improving the resolution of trajectories available and the performance of the wind mapper would likely improve stability of the system.

Another factor discovered which impacted performance is the wind direction estimation. Since the Piccolo heading is driven by the GPS ground track, the heading estimated does not converge until several seconds into flight. If the wind mapper is started before launching the aircraft, the Piccolo attitude filter convergence pollutes the wind direction estimate. Eliminating this effect is the determining factor for the wind map convergence criteria. In finding an appropriate value for the criteria, wind direction errors of greater than 0.2 radians were observed to significantly increase the likelihood of failing to DS. Once dynamic soaring began, the frequent shear crossings gathered enough information to correct the wind direction within 1-2 minutes.

Figure 5.4 illustrates a portion of the flight path flown by the aircraft with a 5 m thick shear of 6 m/s. The trajectory is nominally for an aircraft starting at 24.8 m/s. While some trajectory error can be seen, it follows the path well. In an extended simulation, the aircraft flew in this environmental condition for over 500 cycles before the simulation was terminated. State histories for one cycle of the simulation are illustrated in Figure 5.5.

5.6.2 Light Turbulence

To assess the performance of the dynamic soaring system in a realistic condition, it was tested in a Dryden turbulence field. The MIL-STD-1797A turbulence definitions are used, which defines a range of 20 foot wind magnitude for each turbulence level. Here the high end of the reference wind range is used, defining light turbulence as 10 knots, 5.1 m/s. The standard deviation of the vertical wind is defined as $\sigma_w = 0.1U_{20}$, and horizontal components defined as functions of

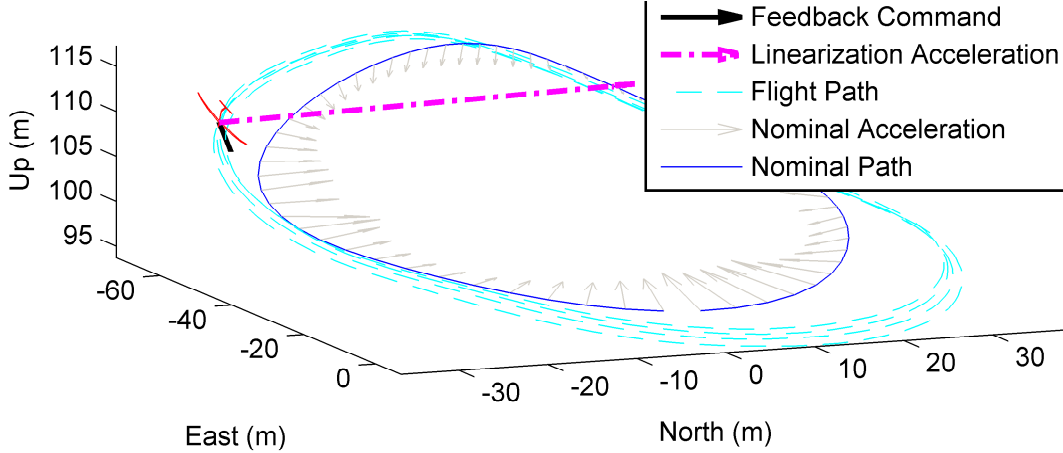


Figure 5.4. Dynamic soaring environment illustrating nominal flight path and acceleration, aircraft pose, and commands (exaggerated for clarity). Flight path is 55 seconds of simulation with shear thickness of 5 m, magnitude of 6 m/s, and no turbulence.

| | Magnitude (m/s) | Length (m) |
|---|-----------------|------------|
| u | 0.88 | 153 |
| v | 0.88 | 153 |
| w | 0.51 | 30 |

Table 5.3. Dryden parameters for light turbulence.

σ_w and height. A reference altitude of 30 m is used here for computing turbulence length scales, turbulence length and intensity is shown in Table 5.3.

Simulations in turbulence revealed the need to plan trajectories with an energy reserve. When soaring without turbulence, the aircraft could fly a trajectory near enough to nominal that an optimal trajectory could be flown, provided that it was not strictly periodic. Eventually the trajectory would stabilize as the aircraft would fly an optimally energy gaining trajectory that became energy neutral after maneuvering losses. With turbulence added, the additional maneuvering and off-nominal C_L from disturbances requires more energy. Planning for a trajectory with a 5% lower than actual airspeed provides energy that significantly improves the reliability of the soaring system in turbulence. Table 5.4 shows that even with this added margin, the turbulent condition favors more energetic trajectories; the 9 m/s, 5 m shear is the only condition to support extended dynamic soaring. Once again, the 12 m/s shear condition destabilized the Piccolo attitude filter to the extent that it was not possible to soar, this was aggravated by the turbulent conditions.

To achieve a direct comparison between dynamic soaring with and without turbulence, a simulation is initialized without turbulence and after five minutes of dynamic soaring, the turbulence is turned on. The path error and changes in energy state between cycles illustrates the effect of the disturbance, shown in Figure 5.6.

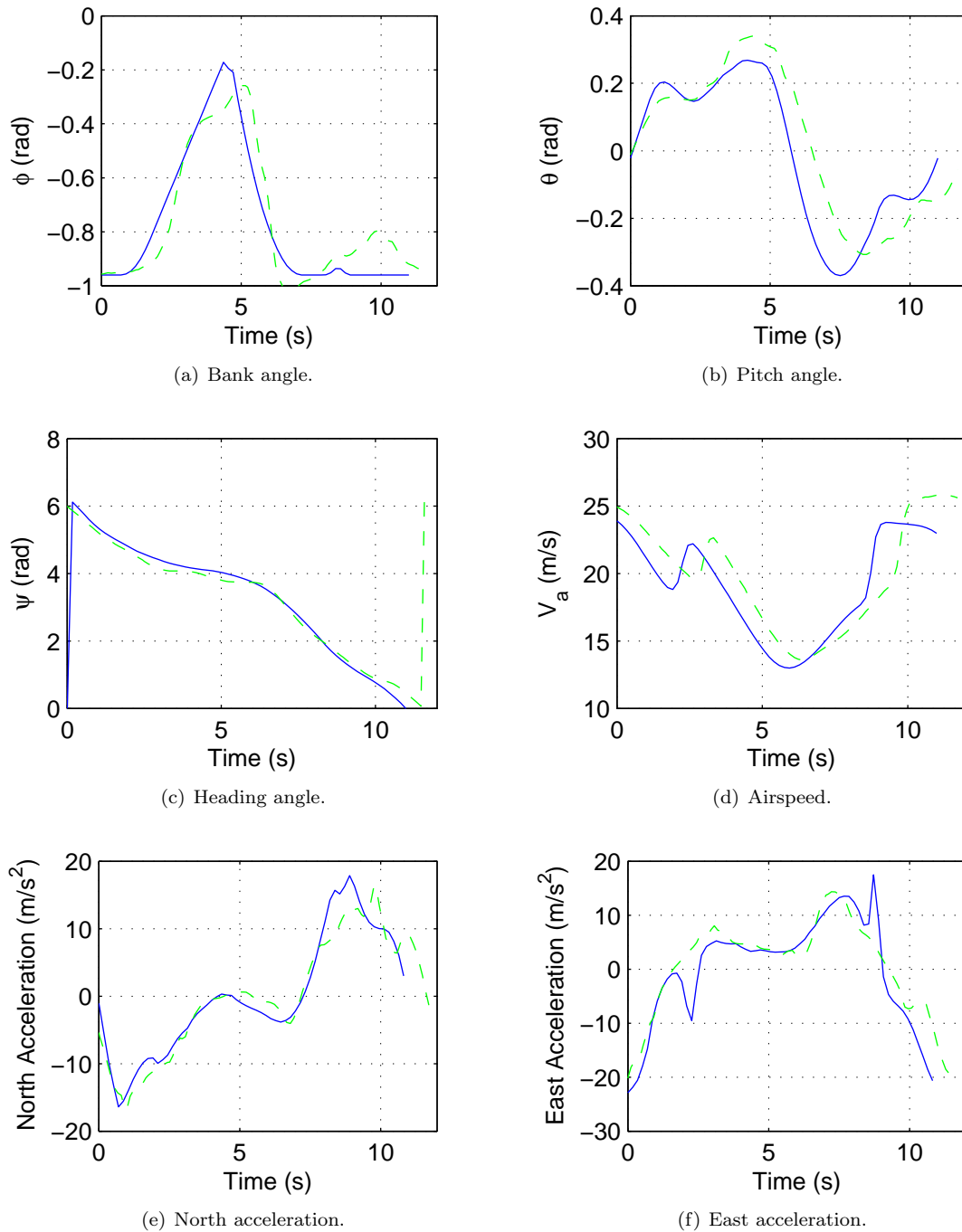
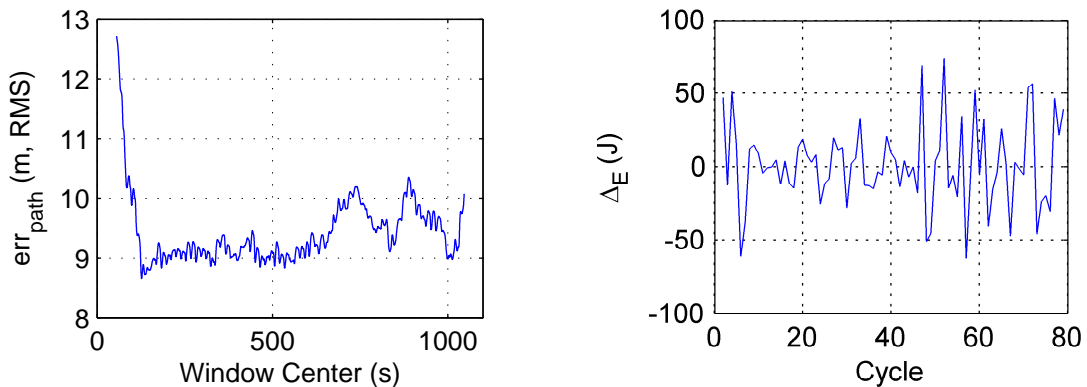


Figure 5.5. Nominal and actual state history for one dynamic soaring cycle. Cycle is planned to start at 24.8m/s in shear with $\Delta h = 5m$, $w = 6m/s$ and no turbulence..

| | | Wind Magnitude | | |
|-----------|------|--------------------|--------------------|--------------|
| | | 6 m/s | 9 m/s | 12 m/s |
| Thickness | 5 m | 25 min | 30 min | Failed to DS |
| | 10 m | 7 min | 5 min | Failed to DS |
| | 20 m | Could Not Maintain | Could Not Maintain | Failed to DS |

Table 5.4. Dynamic soaring system performance in light turbulence. The 12 m/s condition typically failed after the Piccolo attitude filter diverged.



(a) RMS path error computed with a 1000 point sliding window.

(b) Change in energy state between subsequent cycles.

Figure 5.6. Flight path consistency measures, RMS error and energy change between adjacent cycles. Error is computed as the minimum distance between the aircraft location and a point on the flight path, RMS values are computed with a 1000 point sliding window. Simulation is initialized with $\Delta_z = 10$ m, $w=9$ m/s with no turbulence. At approximately $t=600$ seconds, light turbulence is turned on.

5.6.3 Wind Mapper Performance

Performance of the wind mapper in hardware simulation reveals that it works as intended but has deficiencies that prove challenging to continuous dynamic soaring. The under estimated wind shear thickness and magnitude is the most significant and obvious challenge. Several number of factors contribute to this error: the imperfect aircraft aerodynamic model used in wind computations and weak signal in the shear near its limits.

To determine the angle of attack and sideslip to rotate airspeed to inertial axes, a simplified aerodynamic model is used, described in Section 2.4.2, where table Table 2.2 describes the C_L contribution of several neglected factors. As the pitch rate and elevator deflections are both greater than required for steady flight, neglecting these factors could be introducing an error in the wind speed computation. Analysis of these factors is complicated however. The effect of angle of attack error changes sense between ascending and descending legs of the DS cycle. On the ascending leg underestimating the angle of attack will yield a wind measurement smaller than the true wind, while on the descending leg the opposite is true. The pitch rate and elevator effects are also opposite in sense; neglecting pitch rate overestimates angle of attack while neglecting elevator underestimates it.

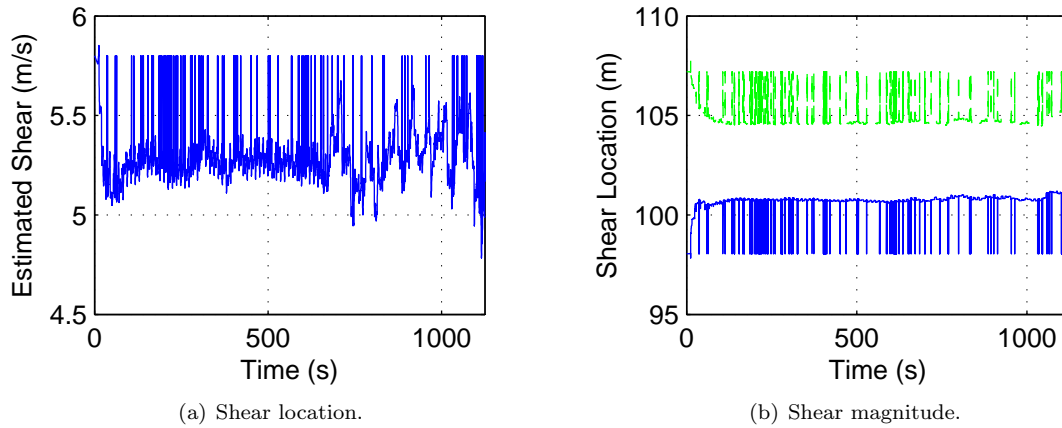


Figure 5.7. Time histories of wind map parameters for $\Delta_z = 5$ m, $w=6$ m/s, shear center is at 102.5 m. Turbulence is turned on at approx 650 seconds. Occasional spikes can be seen that appear to originate in the inter-process communication. Data starts when the dynamic soaring initialization command is issued and does not show wind map convergence prior to start.

Compounding the model error is the fact that at the shear edges, the signal available in the wind profile is weak. For instance, 60% of the wind change occurs in 20% of the shear thickness, and 97% occurs within 60%. Identifying the extent of the shear is thus very difficult, especially in the presence of any noise or modeling error.

Another effect observed in HiL simulation is that occasionally a one sample spike would occur in the wind map. This appears to be an artifact of the IPC, as it is not observed in the wind map data itself but only in the wind map data received by the controller. Wind map performance is illustrated in Figure 5.7.

Conclusions

Endurance and range continues to challenge small UAS, especially in cost-sensitive applications. Birds of similar mass and size realize dramatically superior range and endurance by harvesting energy from vertical velocities and shear in the atmosphere, indicating a means to improve the performance of small UAS. While energy harvesting has been demonstrated for some environmental conditions, UAS still lack the ability to map their atmospheric surroundings in support of energy harvesting.

A means to map the wind field and shear environment has been presented as an enabling technology to harvesting energy from the atmosphere for small UAS. Techniques are developed to map both known and arbitrary environments and to harvest energy from those environments, closing a loop around the energy harvesting problem from environmental mapping to exploitation.

6.1 Use of Wind Maps in Energy Harvesting

6.1.1 Static Soaring

A technique to map arbitrary updraft structures using basis splines is developed. The technique is demonstrated in simulated encounters with convective updrafts, building a map which captures important features of the wind field. A technique to exploit this map is developed and demonstrates performance similar to existing thermalling techniques, and shows resilience to updraft structure and size. An existing path following controller is adapted to the purpose of thermal exploitation, providing the capability to track complex paths through a thermal.

6.1.2 Dynamic Soaring

The wind mapping technique is also applied to dynamic soaring. Using an *a priori* model structure, the mapper estimates features of the shears in lee of ridge environments. This enables selection of an appropriate trajectory for dynamic soaring. The mapper is able to reject turbulent

disturbances and track the shear during dynamic soaring, though the rapid shear crossings and imperfect aircraft model degrades estimates.

A feedback linearization control architecture is developed for dynamic soaring which uses feedforward accelerations to linearize the trajectory and a feedback controller to fly out path errors. The controller is demonstrated to provide trajectory tracking adequate to enable dynamic soaring in several shear environments, though the use of optimal trajectory planning is shown to be problematic, especially for flight in turbulence.. HiL simulations show a COTS autopilot capable of dynamic soaring.

6.2 Recommendations for Future Work

6.2.1 Static Soaring and Wind Maps

Incorporating models for the time evolution of updrafts, such as diffusion-advection equations should be investigated. This could enable the wind map to explicitly model the drift and expansion of thermals through their lifetime, eliminating a source of uncertainty in thermal exploitation. More advanced thermal exploitation algorithms should also be developed which can plan trajectories that for instance, sacrifice climb rate during one portion of a cycle to fly through areas of very strong lift.

In-flight experiments of thermal modeling are also critical to establish that this capability works in the uncertain and complex environment of real thermals, few of which in the author's experience, are shaped like engineering models. Investigation in the application of thermal modeling techniques to cockpit displays for human pilots is also warranted.

6.2.2 Closed-Loop Dynamic Soaring

Autonomous dynamic soaring remains a challenging and relatively unexplored field, a number of challenges that warrant further research were noted in this work.

The Piccolo state estimation filter presents several challenges to dynamic soaring. The large accelerations, rapid turns and altitude changes, and wide speed variation can destabilize the attitude filter. This effect is exacerbated in conditions of strong wind shear (introducing greater disturbances at shear crossing) and turbulence. Attitude filter divergence was found to limit soarable conditions in the more extreme conditions. Future DS systems should have state estimation solutions developed with a focus on reliability during accelerations and large disturbances.

Another challenge the attitude filter posed was in heading bias. Since the heading is derived from GPS track, it is susceptible to errors introduced by wind. Ordinarily these errors would be eliminated as the aircraft turns: the wind components become observable when the aircraft track changes and the heading can be determined. While dynamic soaring however, the wind changes within a single circle. Since the aircraft only turns a single direction, this problem is exacerbated. In order to obtain reliable estimates of the wind direction it was necessary to include a heuristic factor accounting for this discrepancy, a value of 0.06 radians was found to yield satisfactory

results. Future solutions should include a magnetometer or other external heading reference system.

Computing controls that the Piccolo accepts is another source of trajectory error. The longitudinal control especially poses a challenge. Since the Piccolo doesn't perfectly achieve a first order response, the longitudinal tracking has error that often caused the aircraft to overshoot the trajectory low point by up to 4-5 meters. Depending on the terrain surrounding a ridge, this is potentially a tolerable error. When considering boundary layer soaring however, providing sufficient safety margin would make soaring impossible. An operation dynamic soaring system will likely need an autopilot developed for the purpose and providing low-level commands.

Beyond challenges directly posed by the Piccolo, the nature of the paths generated poses a challenge. Computing optimal trajectories is an interesting academic exercise, and provides useful bounds on the potential of dynamic soaring, but optimal paths are not operational ones. In the presence of control errors or turbulence, the aircraft state will not match the optimal state. Energy extraction is then decreased relative to the nominal trajectory and the aircraft will "fall off" the dynamic soaring cycle. Here the problem was handled by planning paths to maximize extraction and selecting a new path at the bottom of each cycle. In this sense, the trajectories were not fully closed in the aircraft state-space, but since they close in geometric space, continuous flight is possible. This approach however, does not always provide enough energy for the aircraft to satisfactorily complete the chosen cycle until the next replan, so paths were selected with a 5% lower initial speed than the aircraft's actual speed. Robust trajectory planning, such as that explored by Flanzer[27] should be investigated in HiL simulation.

Wind estimation during dynamic soaring is another difficulty. Before dynamic soaring, the aircraft can slowly traverse the shear layer to gather information about the structure and width of the shear. During dynamic soaring however, the strongest shear is traversed as rapidly as possible to maximize energy exploitation. The wind mapper is thus modeling with very little information. In simulation, the rapid shear crossing is observed to cause the wind mapper to underestimate the thickness and strength of a shear layer. As these two factors have the opposite effect on energy extracted, the impact on the aircraft is somewhat reduced. The underestimated shear thickness the primary challenge, a heuristic adjustment was used in this work, increasing the thickness by 10%. Further research into the cause of this error is needed, and a trajectory database with higher resolution in environmental conditions should be employed to minimize the effect of mapping errors.

Bibliography

- [1] VAN DER HOVEN, I. (1957) "Power Spectrum of Horizontal Wind Speed in the Frequency Range from 0.0007 to 900 Cycles per Hour," *Journal of Meteorology*, **14**.
URL [http://journals.ametsoc.org/doi/abs/10.1175/1520-0469\(1957\)014%3C0160%3APSOHWS%3E2.0.CO](http://journals.ametsoc.org/doi/abs/10.1175/1520-0469(1957)014%3C0160%3APSOHWS%3E2.0.CO)
- [2] JONES, G. P. I., L. G. PEARSLTINE, and F. H. PERCIVAL (2006) "An assessment of small unmanned aerial vehicles for wildlife research," *Wildlife Society ...*, **34**(3).
URL [http://onlinelibrary.wiley.com/doi/10.2193/0091-7648\(2006\)34\[750:AAOSUA\]2.0.CO;2/abstract](http://onlinelibrary.wiley.com/doi/10.2193/0091-7648(2006)34[750:AAOSUA]2.0.CO;2/abstract)
- [3] LIN, P.-H. (2006) "OBSERVATIONS: The First Successful Typhoon Eyewall-Penetration Reconnaissance Flight Mission Conducted by the Unmanned Aerial Vehicle, Aerosonde," *Bulletin of the American Meteorological Society*, **87**(11), pp. 1481–1483.
URL <http://journals.ametsoc.org/doi/abs/10.1175/BAMS-87-11-1481>
- [4] ELSTON, J. and J. ROADMAN (2011) "The tempest unmanned aircraft system for in situ observations of tornadic supercells: design and VORTEX2 flight results," *Journal of Field ...*, **28**(4), pp. 461–483.
URL <http://onlinelibrary.wiley.com/doi/10.1002/rob.20394/full>
- [5] GARAMONE, J. (2005), "ScanEagle Proves Worth in Fallujah Fight," .
URL <http://www.defense.gov/News/NewsArticle.aspx?ID=24397>
- [6] PENNYCUICK, C. (1982) "The flight of petrels and albatrosses (Procellariiformes), observed in South Georgia and its vicinity," *Philosophical Transactions of the ...*, **300**(1098), pp. 75–106.
URL <http://rstb.royalsocietypublishing.org/content/300/1098/75.short>
- [7] SACHS, G., J. TRAUGOTT, and A. NESTEROVA (2012) "Flying at No Mechanical Energy Cost: Disclosing the Secret of Wandering Albatrosses," *PloS one*, **7**(9).
URL <http://dx.plos.org/10.1371/journal.pone.0041449>
- [8] SHANNON, H. D., G. S. YOUNG, M. A. YATES, M. R. FULLER, and S. SEEGAR (2002) "American White Pelican Soaring Flight Times and Altitudes Relative to Changes in Thermal Depth and Intensity Published by : University of California Press on behalf of the Cooper Ornithological Society Stable URL : <http://www.jstor.org/stable/1370751> ." *The Condor*, **104**(3), pp. 679–683.
- [9] KLAASSEN, M. (1996) "Metabolic constraints on long-distance migration in birds," *The Journal of experimental biology*, **199**(Pt 1), pp. 57–64.
URL <http://www.ncbi.nlm.nih.gov/pubmed/9317335>

- [10] ALLEN, M. (2005) “Autonomous Soaring for Improved Endurance of a Small Uninhabited Air Vehicle,” *Proceedings of the 43rd Aerospace Sciences Meeting, . . .*, pp. 1–13.
URL <http://arc.aiaa.org/doi/pdf/10.2514/6.2005-1025>
- [11] ——— (2007) *Guidance and control for an autonomous soaring UAV, Tech. Rep. April*, NASA Dryden Flight Research Center.
- [12] EDWARDS, D. J. and L. M. SILBERBERG (2010) “Autonomous Soaring: The Montague Cross-Country Challenge,” *Journal of Aircraft*, **47**(5), pp. 1763–1769.
URL <http://arc.aiaa.org/doi/abs/10.2514/1.C000287>
- [13] REICHMANN, H. (1981) *Cross-Country Soaring*.
- [14] DRAKE, V. and R. FARROW (1988) “The Influence of Atmospheric Structure and Motions on Insect Migration,” *Annual Review of Entomology*, **33**, pp. 183–210.
- [15] RAYLEIGH, L. (1883) “The Soaring of Birds,” *Nature*, **27**(701), pp. 534–535.
- [16] ANDERSSON, K., I. KAMINER, V. DOBROKHODOV, and V. CICHELLA (2012) “Thermal Centering Control for Autonomous Soaring; Stability Analysis and Flight Test Results,” *Journal of Guidance, Control, and Dynamics*, **35**(3), pp. 963–975.
URL <http://arc.aiaa.org/doi/abs/10.2514/1.51691>
- [17] MACCREADY, P. B. J. (1958) “Optimum Airspeed Selector,” *Soaring*, (1), pp. 10–11.
- [18] GRUBIŠIĆ, V. and B. J. BILLINGS (2008) “Climatology of the Sierra Nevada Mountain-Wave Events,” *Monthly Weather Review*, **136**(2), pp. 757–768.
URL <http://journals.ametsoc.org/doi/abs/10.1175/2007MWR1902.1>
- [19] NIELSEN, J. W. (1992) “In Situ Observations of Kelvin-Helmholtz Waves along a Frontal Inversion,” *Journal of the Atmospheric Sciences*, **49**(5), pp. 369–386.
- [20] CHAKRABARTY, A. and J. W. LANGELAAN (2011) “Energy-Based Long-Range Path Planning for Soaring-Capable Unmanned Aerial Vehicles,” *Journal of Guidance, Control, and Dynamics*, **34**(4), pp. 1002–1015.
URL <http://arc.aiaa.org/doi/abs/10.2514/1.52738>
- [21] KLEMPERER, W. (1958) “A Review on the Theory of Dynamic Soaring,” *Technical Soaring*.
URL <http://scholar.google.com/scholar?hl=en&btnG=Search&q=intitle:A+Review+of+the+Theory+of>
- [22] WOOD, C. (1973) “The flight of albatrosses (a computer simulation),” *Ibis*, pp. 244–256.
URL <http://onlinelibrary.wiley.com/doi/10.1111/j.1474-919X.1973.tb02640.x/full>
- [23] (2013), “RC Speeds: Fastest 20 Aircraft,” .
URL <http://rcspeeds.com/aircraft.aspx?AirplaneType=BD>
- [24] SACHS, G. and O. DA COSTA (2006) “Dynamic soaring in altitude region below jet streams,” *AIAA Guidance, Navigation, and Control Conference*, (August), pp. 1–11.
URL <http://arc.aiaa.org/doi/pdf/10.2514/6.2006-6602>
- [25] GRENESTEDT, J. L. and J. R. SPLETZER (2010) “Towards Perpetual Flight of a Gliding Unmanned Aerial Vehicle in the Jet Stream,” *IEEE Conference on Decision and Control*.
- [26] SUKUMAR, P. and M. SELIG (2010) “Dynamic Soaring of Sailplanes over Open Fields,” (July).
URL <http://arc.aiaa.org/doi/pdf/10.2514/6.2010-4953>

- [27] FLANZER, T. C., G. C. BOWER, and I. M. KROO (2012) “Robust Trajectory Optimization for Dynamic Soaring,” *AIAA Guidance, Navigation, and Control Conference*, (August), pp. 1–22.
- [28] SACHS, G. (2005) “Minimum shear wind strength required for dynamic soaring of albatrosses,” *Ibis*, **147**, pp. 1–10.
URL <http://onlinelibrary.wiley.com/doi/10.1111/j.1474-919x.2004.00295.x/full>
- [29] ZHAO, Y. J. (2004) “Optimal patterns of glider dynamic soaring,” *Optimal Control Applications and Methods*, **25**(2), pp. 67–89.
URL <http://doi.wiley.com/10.1002/oca.739>
- [30] ZHAO, Y. J. and Y. C. QI (2004) “Minimum fuel powered dynamic soaring of unmanned aerial vehicles utilizing wind gradients,” *Optimal Control Applications and Methods*, **25**(5), pp. 211–233.
URL <http://doi.wiley.com/10.1002/oca.744>
- [31] DEITERT, M., A. RICHARDS, C. A. TOOMER, and A. PIPE (2009) “Engineless Unmanned Aerial Vehicle Propulsion by Dynamic Soaring,” *Journal of Guidance, Control, and Dynamics*, **32**(5), pp. 1446–1457.
URL <http://arc.aiaa.org/doi/abs/10.2514/1.43270>
- [32] FLANZER, T., R. BUNGE, and I. KROO (2012) “Efficient Six Degree of Freedom Aircraft Trajectory Optimization with Application to Dynamic Soaring,” (September), pp. 1–19.
URL <http://arc.aiaa.org/doi/pdf/10.2514/6.2012-5622>
- [33] BOSLOUGH, M. (2002) *Autonomous dynamic soaring platform for distributed mobile sensor arrays, Tech. rep.*, Sandia National Laboratories.
URL <https://cfwebprod.sandia.gov/cfdocs/CCIM/docs/02-1896.MobileSensorArrays.pdf>
- [34] BOWER, G. (2011) “Boundary Layer Dynamic Soaring for Autonomous Aircraft: Design and Validation,” (December).
URL <http://scholar.google.com/scholar?hl=en&btnG=Search&q=intitle:BOUNDARY+LAYER+DYNAMIC+SO>
- [35] PARK, S. (2011) “Autonomous Aerobatic Flight by Three-Dimensional Path-Following with Relaxed Roll Constraint,” *AIAA Guidance, Navigation and Control Conference*, (August), pp. 1–14.
URL <http://arc.aiaa.org/doi/pdf/10.2514/6.2011-6593>
- [36] GORDON, R. J. (2006) *Optimal Dynamic Soaring for Full Size Sailplanes*, Ph.D. thesis, Air Force Institute of Technology.
- [37] PHILLIPS, W. H. (1975) “Propulsive Effects due to Flight through Turbulence,” *Journal of Aircraft*, **12**(7), pp. 624–626.
- [38] PATEL, C. K. and I. KROO (2006) “Control Law Design for Improving UAV Performance Using Wind Turbulence,” *AIAA Aerospace Sciences Meeting*, (January), pp. 1–10.
- [39] LANGELAAN, J. W. (2009) “Gust Energy Extraction for Mini and Micro Uninhabited Aerial Vehicles,” *Journal of Guidance, Control, and Dynamics*, **32**(2), pp. 464–473.
URL <http://arc.aiaa.org/doi/abs/10.2514/1.37735>
- [40] DEPENBUSCH, N. (2011) “Atmospheric Energy Harvesting for Small Uninhabited Aircraft by Gust Soaring,” (August).
URL http://www.aero.psu.edu/avia/pubs/Depenbusch_MS.pdf

- [41] PENNYCUICK, C. (2002) “Gust soaring as a basis for the flight of petrels and albatrosses (Procellariiformes),” *Avian Science*, **2**(1), pp. 1–12.
URL <http://www.eouunion.org/pdf/v21/AS-2-1-Pennycuick.pdf>
- [42] EDWARDS, D. J. (2008) “Implementation Details and Flight Test Results of an Autonomous Soaring Controller,” *AIAA Guidance, Navigation and Control Conference*.
- [43] BARATE, R., S. DONCIEUX, and J.-A. MEYER (2006) “Design of a bio-inspired controller for dynamic soaring in a simulated unmanned aerial vehicle.” *Bioinspiration & biomimetics*, **1**(3), pp. 76–88.
URL <http://www.ncbi.nlm.nih.gov/pubmed/17671309>
- [44] CONE, C. (1964) *The design of sailplanes for optimum thermal soaring performance*, *Tech. Rep. January*, NASA Langley Research Center.
URL <http://scholar.google.com/scholar?hl=en&btnG=Search&q=intitle:The+Design+of+Sailplanes+>
- [45] KONOVALOV, D. (2005) “On the Structure of Thermals,” *Technical Soaring*, **29**(4).
- [46] ——— (1970) “On the Structure of Thermals,” in *OSTIV Publication XI*, OSTIV, Alpine, TX.
- [47] GEDEON, J. (1976) “The Influence of Sailplane Performance and Thermal Strength on Optimal Dolphin-Flight Transition Piloting Techniques,” *Technical Soaring*, **XIV**.
- [48] PROJECT, X. (2012), “XCSoar 6.3,” .
- [49] LANGELAAN, J. W., J. SPLETZER, C. MONTELLA, and J. GRENESTEDT (2012) “Wind field estimation for autonomous dynamic soaring,” *2012 IEEE International Conference on Robotics and Automation*, (c), pp. 16–22.
URL <http://ieeexplore.ieee.org/lpdocs/epic03/wrapper.htm?arnumber=6224954>
- [50] PROCTOR, F. H., D. A. HINTON, and R. L. BOWLES (2000) “A Windshear Hazard Index,” *AMS Conference on Aviation, Range, and Aerospace Meteorology*.
- [51] STEVENS, B. L. and F. L. LEWIS (2003) *Aircraft Control and Simulation*, 2nd ed., Wiley, Hoboken, New Jersey.
URL <http://www.worldcat.org/oclc/51751879>
- [52] (2010) *FOX Assembly Instructions*, *Tech. rep.*, EScale.
- [53] HOBLIT, F. M. (1988) *Gust Loads on Aircraft: Concepts and Applications*, 1 ed., American Institute of Aeronautics and Astronautics, Washington, DC.
- [54] MOORHOUSE, D. and R. WOODCOCK (1982) “Background Information and User Guide for MIL-F-8785C, Military Specification-Flying Qualities of Piloted Airplanes,” .
URL <http://oai.dtic.mil/oai/oai?verb=getRecord&metadataPrefix=html&identifier=ADA119421>
- [55] LANGELAAN, J. W., N. ALLEY, and J. NEIDHOEFER (2011) “Wind Field Estimation for Small Unmanned Aerial Vehicles,” *Journal of Guidance, Control, and Dynamics*, **34**(4), pp. 1016–1030.
URL <http://arc.aiaa.org/doi/abs/10.2514/1.52532>
- [56] MYSCHIK, S., M. HELLER, F. HOLZAPFEL, and G. SACHS (2004) “Low-Cost Wind Measurement System for Small Aircraft,” *AIAA Guidance, Navigation, and Control Conference*, (August), pp. 1–10.

- [57] HOUTEKAMER, P. L. and H. L. MITCHELL (1998) “Data Assimilation Using an Ensemble Kalman Filter Technique,” *Monthly Weather Review*, **126**, pp. 796–811.
- [58] SIMON, D. (2006) *Optimal State Estimation: Kalman, H Infinity, and Nonlinear Approaches*, Wiley.
- [59] THRUN, S., W. BURGARD, and D. FOX (2005) *Probabilistic Robotics*, MIT Press, Cambridge.
- [60] PANOFSKY, H. A., A. K. BLACKADAR, and G. E. MCVEHIL (1960) “The diabatic wind profile,” *Quarterly Journal of the Royal Meteorological Society*, **86**(369), pp. 390–398.
- [61] BELCHER, S. and J. HUNT (1998) “Turbulent Flow over Hills and Waves,” *Annual Review of Fluid Mechanics*, **30**, pp. 507–538.
- [62] WOOD, N. (1995) “The Onset of Separation in Neutral Turbulent Flow Over Hills,” *Boundary-Layer Meteorology*, **76**, pp. 137–164.
- [63] GRANT, A. and P. MASON (1990) “Observations of boundary-layer structure over complex terrain,” *Quarterly Journal of the Royal Meteorological Society*, **116**(491), pp. 159–186.
URL <http://dx.doi.org/10.1002/qj.49711649107>
- [64] FARRUGIA, R. (2003) “The wind shear exponent in a Mediterranean island climate,” *Renewable Energy*, **28**(4), pp. 647–653.
URL <http://linkinghub.elsevier.com/retrieve/pii/S0960148102000666>
- [65] DIERCX, P. (1993) *Curve and Surface Fitting with Splines*, Oxford University Press.
- [66] DE BOOR, C. (1978) *A Practical Guide to Splines*, Springer-Verlag New York.
- [67] PACHTER, M., N. CECCARELLI, and P. R. CHANDLER (2008) “Estimating MAVs Heading and the Wind Speed and Direction Using GPS, Inertial, and Air Speed Measurements,” *AIAA Guidance, Navigation, and Control Conference*.
- [68] ANDERSSON, K. and I. KAMINER (2009) “On Stability of a Thermal Centering Controller,” *AIAA Guidance, Navigation and Control Conference*, (August), pp. 1–15.